

The Pennsylvania State University
The J. Jeffrey and Ann Marie Fox Graduate School

**USING THE ICE CRYSTAL TRAJECTORY GROWTH (ICTG) MODEL IN
TROPICAL CYCLONES: UNIQUE AND EXTREME ICE CRYSTAL
PATHWAYS IN HURRICANE HARVEY**

A Thesis in
Meteorology and Atmospheric Science
by
Matthew J. Varela

© 2025 Matthew J. Varela

Submitted in Partial Fulfillment
of the Requirements
for the Degree of

Master of Science

December 2025

The thesis of Matthew J. Varela was reviewed and approved by the following:

Anthony C. Didlake Jr.
Associate Professor of Meteorology
Thesis Advisor

Jerry Harrington
Associate Head and Professor of Meteorology

Yunji Zhang
Assistant Professor of Meteorology and Atmospheric Science

Paul Markowski
Department Head and Distinguished Professor of Meteorology

Abstract

Accurately modeling ice microphysics remains challenging because there are numerous complex sub-grid scale processes involved. In an effort to reduce these errors and improve our scientific understanding, a new Lagrangian model was developed by Laurencin et al. (2022).

The Ice Crystal Trajectory Growth (ICTG) model uses a Lagrangian framework to follow individual ice crystals and their growth processes through a storm simulated separately in an Eulerian model. This Lagrangian approach provides a more detailed representation of the wide variety of ice crystals and their properties. In this project, we use the ICTG model to study ice microphysics in a tropical cyclone (TC) eyewall. We use a simulation of Hurricane Harvey (2017) that was run using the Weather Research and Forecasting (WRF) model initialized using the Pennsylvania State University Ensemble Kalman Filter (PSU-EnKF) system.

Typical crystal pathways are those crystals that are lofted by an updraft, grow to a large size and start to sink quickly, and then melt once reaching the melting level. The research here focuses on unique particles, including those that make more than one full revolution around the TC, and extreme crystals, including those with high particle mass ($> 100 \text{ mg}$) and low particle aspect ratio ($< 5.5 \times 10^{-2}$). This allows us to better understand the full range of possibilities for an ice crystal in a TC.

Some key findings include that the updrafts present within a TC can cause extreme crystal diversity, such as crystals able to reach far radial distances. Updrafts act as a trigger, amplifying small initial differences and producing divergent outcomes based on whether a crystal enters the updraft, the timing of entering the updraft, and/or its mass. In addition, a crystal's initial size and/or location within a storm azimuthally, radially, and vertically has major impacts on its behavior over time. These new findings and potential improvements to ice microphysics in weather forecast models will aid in predictions of intensity and structural changes of TCs.

Table of Contents

List of Figures	v
List of Tables	viii
Acknowledgments	ix
Chapter 1 Introduction	1
Chapter 2 Data and Methods	6
2.1 Hurricane Harvey Weather Research and Forecasting Ensemble Kalman Filter (WRF-EnKF) Simulation Background	6
2.2 Ice Crystal Trajectory Growth (ICTG) Model Background	8
2.3 Ice Crystal Initialization and Model Integration	10
Chapter 3 Results	14
3.1 Extreme Crystals- Largest Mass and Lowest Aspect Ratio	16
3.2 Unique Crystals- One or More Revolutions	22
3.3 Multiple Unique and Extreme Crystals	31
Chapter 4 Conclusions	47
Bibliography	50

List of Figures

2.1	Model intensity (a) depicts maximum wind speed in light red, 60-minute average of maximum wind speed in dark red, and minimum sea level pressure in blue. The vertical red line marks the time of analysis- 0400 UTC 25 August 2017. Model Storm Center Track (b) uses 1km wind center tracks marked at every 3 hours. The red point denotes the time of analysis.	7
2.2	Figure adapted from Laurencin et al. (2022) Figures 5 and 6. Ice crystal trajectories are simulated within a leading-convective trailing-stratiform squall line. Crystals are initialized within the gray square, trajectory density is shaded, and reflectivity and vertical velocity are contoured (a-d). Time series of crystal properties shown in e-i	10
2.3	Frequency distribution of crystal initialization locations by altitude (a). 818 locations selected for crystal initialization based on noted criteria. (b) IWC Distribution and (c) Number Concentration by Size Bin displays the source model microphysical information for a single initialization location. Vertical colored lines in (b) and (c) show the 5 selected crystal initial sizes based on the IWC percentiles.	11
2.4	Simulated Radar Reflectivity Plan Views for Hurricane Harvey at 2 km altitude. All crystals are initialized at blue dots (a). Crystals analyzed here are initialized at red dots (a). All crystal trajectories for the middle size bin at each initialization location (b). Vertical Velocity Plan View for Hurricane Harvey at 6 km altitude (c) with shear quadrants and shear heading denoted.	12
3.1	Crystals are initialized at the dots. Colored trajectories denote different extreme crystals that meet the specified criteria- largest mass crystals in (a), (b), (c), and (d) and lowest aspect ratio crystals in (e), (f), and (g). Reflectivity in (a) and (e) at 6.5 km altitude.	16

3.2	Crystals are initialized at the dot. Colored trajectories denote different initial size bins. Gray trajectories are other crystals initialized within the yellow box (d). Reflectivity in (a) at 6.5 km altitude. Shear quadrants are marked in (d). Black dashed lines and colored markers denote 2600 seconds and 3500 seconds when further analysis occurs.	19
3.3	Crystals are initialized at the black dot in (a). Colored trajectories denote different initial size bins. Reflectivity in (a) at 6.5 km altitude. Azimuthal cross section (b) with vertical velocity radially averaged between 15 km and 35 km radius. Radial cross sections along dashed lines in (a and b) at 200° azimuth (c and d) and 175° azimuth (e and f).	21
3.4	Crystals are initialized at the dots. Colored trajectories denote different extreme crystals that meet the specified criteria. Reflectivity in (a) at 6.5 km altitude. Shear quadrants are marked in (d).	23
3.5	As in Figure 3.2 for a different initialization location. Black dashed lines and colored markers denote 1040 seconds, 1440 seconds, and 4700 seconds when further analysis occurs.	26
3.6	Crystals are initialized at the dot. Colored trajectories denote different initial size bins. Reflectivity in (a) at 6.5 km altitude. Azimuthal cross section (b) with tangential velocity radially averaged between 13 km and 18 km radius. Radial cross sections (c and d) along dashed lines in (a and b) at 295° azimuth (1040 seconds) and 268° azimuth (1440 seconds).	28
3.7	Crystals are initialized at the dot. Colored trajectories denote different initial size bins. Reflectivity in (a) at 6.5 km altitude. Radial cross sections (b, c, and d) along dashed lines in (a) at 110° azimuth, 123° azimuth, and 126° azimuth (4700 seconds). Tangential winds contoured at every 5 m/s.	30
3.8	Crystals are initialized at the dot. Colored trajectories denote different initial size bins. Colored markers denote times when further analysis occurs. Reflectivity in (a) at 6.5 km altitude. Shear quadrants are marked in (d).	32
3.9	Crystals are initialized at the dot. Colored trajectories and markers denote different initial size bins. Reflectivity in (a) at 6.5 km altitude. Azimuthal cross section (b) with vertical velocity radially averaged between 22.5 km and 32.5 km radius. Radial cross sections (c, d, e, f) along dashed lines in (a) at 136° azimuth (0 seconds) in c and d and 113° azimuth (1400 seconds) in e and f.	34

3.10 Crystals are initialized at the dot. Colored trajectories and markers denote different initial size bins. Reflectivity in (a) at 6.5 km altitude. Azimuthal cross section (c) with tangential velocity radially averaged between 25 km and 35 km radius. Radial cross sections (b and d) along dashed line in (a) at 94° azimuth (3100 seconds) in b and 65° azimuth (5580 seconds) in d. Radial velocity contoured at every 5 m/s in (b) and (d).	35
3.11 Crystal is initialized at the dot. Blue trajectories and markers denotes crystal initialized at size bin 1 (FC4). Reflectivity in (a) at 6.5 km altitude. Radial cross sections (b, c, and d) along dashed lines in (a) at 110° azimuth (7600 seconds) in b, 106° azimuth (15000 seconds) in c, and 98° azimuth (18000 seconds) in d. Tangential winds contoured at every 5 m/s in b, c and d.	37
3.12 Crystal is initialized at the dot. Red trajectories and markers denotes crystal initialized at size bin 2 (FC5). Reflectivity in (a) at 6.5 km altitude. Radial cross sections (b-g) along dashed lines in (a) at 56° azimuth (7000 seconds) in b and c, 42° azimuth (8500 seconds) in d and e, and 105° azimuth (10300 seconds) in f and g. Vertical velocity contoured at every 1 m/s in c, e, and g.	39
3.13 Crystal is initialized at the dot. Green trajectories and markers denotes crystal initialized at size bin 3 (FC6). Reflectivity in (a) at 6.5 km altitude. Vertical Velocity radial cross section (b) is along dashed line in (a) originating at the center of TC. Azimuthal cross section (c) with tangential velocity radially averaged between 25 km and 40 km radius. Vertical Velocity south to north cross section (d) is along dashed line in (a) running from south to north.	40
3.14 Crystals are initialized at the dot. Colored trajectories denote different initial size bins. Reflectivity in (a) at 6.5 km altitude. Shear quadrants are marked in (f).	41
3.15 Crystals are initialized at the dots. Colored trajectories denote crystals- Crystal 14 and Crystal 15 in (a-f) and Crystal 16 and FC6 in (g-l). Reflectivity in (a) and (g) at 6.5 km altitude. Radial cross sections in Figure 3.16 are along dashed lines in (a) and (g) at 93° azimuth and 91° azimuth. Shear quadrants are marked in (e) and (k).	43
3.16 Crystals are initialized at the dots. Colored trajectories and markers denote different initial size bins. Azimuthal cross section (b) with tangential velocity radially averaged between 25 km and 35 km radius. Dashed line in (b) denotes 0 m/s tangential velocity. Radial cross sections (a and c) at 93° azimuth in (a) and 91° azimuth in (c). Radial velocity contoured at every 5 m/s in (a) and (c).	44

List of Tables

2.1	Extreme and Unique Crystal Categories identified and analyzed in this study	13
3.1	Unique/Extreme Characteristic(s), size bin, initial mass (in mg), and figure references for selected crystals.	15

Acknowledgments

I am deeply grateful to my advisor, Dr. Anthony Didlake Jr., for his invaluable guidance and support throughout my research at Penn State. I also sincerely appreciate my committee members, Drs. Jerry Harrington and Yunji Zhang, and Bruno Rojas for their insightful feedback and perspectives. Additionally, I would like to thank my family, friends, and colleagues for their unwavering encouragement and support during these last two years.

This material is based upon work supported by NASA Award No. 80NSSC22K0613. Any opinions, findings, and conclusions or recommendations expressed in this publication are those of the author(s) and do not necessarily reflect the views of NASA.

Chapter 1

Introduction

Weather forecast models have remarkably improved over the past several decades, but several shortcomings still limit forecast accuracy of organized convection. One such shortcoming is the accurate representation of ice microphysical processes in models. Modeling microphysics remains challenging due, in part, to the numerous and complex sub-scale processes involved. The representation of these processes in weather forecast models often includes large and faulty assumptions, such as having a fixed particle size distribution and/or using fixed intercept and slope parameters. This can lead to significant errors in these models. These errors are evident in how simulated storms respond to the chosen microphysics parameterization scheme used in forecast models. The chosen scheme can significantly influence the structure of simulated organized convection, including squall lines and tropical cyclones (TCs) (e.g., Morrison et al., 2009; Bryan and Morrison, 2012; Morrison et al., 2012, 2020). In this thesis, we examine a new microphysics model—specifically focused on ice microphysical processes—applied to tropical cyclones.

Modeling ice microphysics remains more challenging than modeling warm micro-physics due to the complexity of subgrid-scale processes involved. Warm-phase processes largely involve spherical or oblate liquid droplets with better-known mass-fall speed relationships. In contrast, ice-phase processes must account for a wide range of ice crystal habits, including columns, plates, dendrites, and aggregates, that evolve with changes in temperature and humidity. Heymsfield et al. (2006) conducted in-situ measurements during Hurricane Humberto and found high concentrations of small ice particles within the eyewall updrafts. The slope parameter of the fitted exponential size distributions (λ) was notably lower near the eye ($\lambda < 30 \text{ cm}^{-1}$), indicating high temperature growth processes, while higher λ values outside the eyewall ($\lambda > 100 \text{ cm}^{-1}$) suggested lower

temperature growth conditions due to slower growth. These findings suggest that, despite some similarities, hurricane ice microphysics exhibit unique characteristics that may require specialized treatment in weather models. Variations in ice crystal habits, along with their impact on physical properties, highlight the challenges of accurately modeling ice microphysics in weather forecast models.

Varying ice crystal shapes influence key properties like fall speed and mass, making accurate representation in models particularly difficult. These behaviors all have downstream impacts on the precipitation, including its intensity and location (Woods et al., 2007). Additionally, Mason (1994) finds several effects based on the modeled ice crystal shape. Most numerical weather prediction models assume that ice is spherical or use mass-size relationships. The ice crystal shape can affect the cloud albedo and therefore the radiation budget. Other effects of the crystal shape and behavior include the collection efficiency for riming and the time to sublimation. Mason (1994) also found that columns and needles are more likely to grow rapidly than plates due to their much higher collection efficiency for supercooled droplets. They are able to better catch supercooled droplets which freeze on contact. Finally, more complex ice crystal shapes have a greater mass than the less complex shapes when falling at the same vertical levels. This greater mass occurs because they fall more slowly and thus take a longer time to move between these levels, allowing them to grow larger. For the above reasons, modeling the ice shape correctly matters in numerical weather prediction and spherical growth is not an ideal assumption.

Currently, the vast majority of microphysics modeling in weather forecast models use an Eulerian approach for modeling ice microphysics. In this approach, a model predicts changes to variables at fixed points in space, tracking the collective properties (e.g., shape, density, fall speed) of a group of ice particles within a grid box volume. The values at a point area are a grid box average. In this manner, average properties are retained during the simulation, while deviations are lost. Both bulk and bin microphysics schemes use the Eulerian approach, but with different assumptions and different extents of averaging of particle characteristics within a grid volume. Bulk microphysics schemes represent hydrometeors using averaged properties, such as mass and number concentration (e.g., Morrison et al., 2015), while bin schemes explicitly resolve the particle size distribution by dividing it into discrete size bins (Khain et al., 2015).

In most bulk microphysics schemes, ice particles are artificially categorized into classes. These classes generally represent different hydrometeor types, such as graupel, snow, and

ice. Particles then move through these classes using criteria that are usually arbitrary (Harrington et al., 2013). Recent advancements in modeling approaches have shifted towards predicting the continuous evolution of particle properties rather than relying on discrete classes, which allows a more natural evolution of the particle's properties. One such scheme was created by Hashino and Tripoli (2007). The Spectral Ice Habit Prediction System (SHIPS) allows solid hydrometeors to have evolving characteristics. Another scheme by Jensen et al. (2017) predicts the evolution of ice properties and is called the Ice-Spheroids Habit Model with Aspect-Ratio Evolution (ISHMAEL) scheme. The Predicted Particle Properties (P3) scheme is another scheme that predicts the evolution of ice properties. It does not have conversions between particle types, which is generally used in traditional schemes (Morrison and Milbrandt, 2015; Morrison et al., 2015). Instead, it uses "free" ice categories. The P3 scheme continues to be improved in recent years by having an explicit description of wet snow and ice pellets, for instance (Cholette et al., 2019).

In order to further improve ice modeling, Lagrangian schemes have recently been developed. These approaches have several advantages over Eulerian methods. Importantly, they allow individual crystal tracking, offering a more explicit representation of ice crystals and their growth processes, such as vapor deposition and riming, compared to the Eulerian approach (Grabowski et al., 2019). This method provides a more detailed and dynamic representation of the diverse range of ice crystals and their evolving properties throughout a simulation. By modeling each particle individually, Lagrangian approaches offer a more precise representation of ice microphysical processes, leading to improved accuracy in simulating ice crystals. McSnow, developed by Brdar and Seifert (2018), is one Lagrangian model focusing on deposition, riming, aggregation, and sedimentation and uses a so-called "super-droplet" method. Jensen et al. (2018) use Lagrangian schemes to track ice crystals advected from the tops of deep convection. Additionally, Kumjian and Lombardo (2020) use a Lagrangian scheme in their microphysical model of hail growth to track hailstones.

Accurately forecasting TCs depends heavily on our understanding and modeling of ice microphysics, with Lagrangian approaches having valuable insights. Our current understanding heavily relies on in-situ observations, ground-based radar, and airborne Doppler radars (e.g., Black and Hallett, 1986; Marks and Houze, 1987), though each has limitations. Early research relied on in-situ airborne observations that examined ice particle type and concentration in the inner core (e.g., Black, 1990; Black and

Hallett, 1986, 1999), and showed that ice particle distributions vary across storm regions (e.g., Houze et al., 1992; Marks and Houze, 1987). In-situ observations only provide snapshots of a crystal's evolution (e.g., Houze and Churchill, 1984; Black and Hallett, 1986). Reconnaissance aircraft generally only fly through regions of light or stratiform precipitation, where vertical motions are weak and safer for aircraft. Aircraft typically avoid the intense vertical motions in the eye and eyewall regions, where cold-phase processes dominate (Houze, 2010). Ground-based dual-polarization radars have helped fill some of these gaps (e.g., Didlake and Kumjian, 2017; Huang et al., 2022; Laurencin et al., 2020, 2022; Rojas et al., 2025), but they still require validation with in-situ observations to get the exact characteristic data of the ice crystals. Though there are observational challenges, studies using polarimetric radar have revealed key features, such as melting hail and graupel in the eyewall of TC Ingrid and snow and ice crystals in the outflow (May et al., 2008). Despite these advancements, the complexity of ice-phase processes in TCs continues to challenge both observational efforts and microphysics modeling, particularly within the critical eye and eyewall regions.

The Ice Crystal Trajectory Growth (ICTG) model, developed by Laurencin et al. (2022), represents a unique advancement in ice crystal modeling, particularly by using the Lagrangian approach to model representation. The model grows and advects individual ice crystals and tracks the evolving ice crystal properties for these crystals. Additionally, the model calculates the properties of the ice crystals (e.g. axis lengths, effective density, and fall speed) at small time intervals for a selected time length over the trajectory lifetime. The ICTG is a unique and novel model for several reasons. First, it uses lab-based parameterizations for growth by vapor deposition (Harrington et al., 2019; Zhang and Harrington, 2014) and riming (Jensen and Harrington, 2015) that account for adaptive habit behavior. The model uses strategically selected assumptions (e.g., the ICTG is run offline and does not feed back into the source model) that allows minimal computing cost.

The ICTG model was first applied to a leading-convective trailing-stratiform squall line in Oklahoma on 19 June 2007 and produced realistic crystal growth properties as noted in Laurencin et al. (2022). The authors conducted both two- and three-dimensional simulations. Laurencin et al. (2022) found that, in general, smaller crystals were transported rearward into the trailing stratiform region, while larger crystals did not travel as far and fell out primarily in the leading convective line. This implied that the ICTG was successfully simulating the basics of ice growth and size sorting in an idealized representation of organized convection.

Several enhancements have been made to the ICTG model following its implementation in Laurencin et al. (2022). Previously, the ICTG model initialized ice crystals at prescribed sizes at all locations within a volume. The initialization method, described in more detail in Chapter 2, has been improved to initialize ice crystals in locations that are favorable for the generation of new ice crystals. Additionally, rather than discretely chosen initialization sizes, the initialization sizes are based on the ice water content (IWC) distribution at that particular location.

The ICTG model has also recently been applied to a TC eyewall (Harvey (2017)) in Rojas et al. (2025) as an extension of Laurencin et al. (2022). This hurricane serves as a particularly impactful case study for modeling ice crystal processes within TCs, due to its extreme rainfall totals, which caused widespread and long-lasting societal impacts across the Texas Gulf Coast. Rojas et al. (2025) found that riming was limited to low-altitude crystals and the largest ice crystals were initialized in the dendritic growth zone. This thesis is an extension of Rojas et al. (2025) and will also apply the ICTG model to the eyewall region of Hurricane Harvey. We will analyze how both the ice crystal environment and the ice crystal properties evolve over time. Rojas et al. (2025) performed a broad analysis of all modeled eyewall crystals. By contrast, this paper focuses on unique and extreme individual ice crystals to better understand the full range of possibilities for an ice crystal initialized in a TC eyewall. Furthermore, the study will investigate the effect that spatial variations of an ice crystal's environment and an ice crystal's initial size have on the overall evolution of the ice crystal's trajectory and properties.

Thus, we believe that the ICTG model will show that small spatial variations within the environment and the initial crystal size will create varied trajectory paths and differing crystal properties. This research will add to our current understanding of modeling ice microphysics within TCs as forecasting TCs is highly dependent on how ice microphysics are modeled. Trajectory modeling of ice crystals is important because the location of where crystals grow can affect where in the hurricane latent heat release and latent cooling occurs which, in turn, can affect the overall strength, intensity, and structure of the TC.

Chapter 2 covers the data and methods used in this study. Chapter 3 will show the results, including a look at three different sets of ice crystals from our simulation. Finally, the conclusions will be presented in Chapter 4.

Chapter 2

Data and Methods

Hurricane Harvey originated as a wave that moved off the west coast of Africa on 12 August 2017. The storm rapidly intensified in the Gulf of Mexico and became an intense Category 4 hurricane just prior to landfall. It made landfall on the Texas Gulf Coast near Rockport, Texas, at 0300 UTC 26 August 2017 (Blake and Zelensky, 2018).

Overall, there are two models used in this analysis. The first is the Weather Research and Forecasting (WRF) Model version 3.8.1 (Skamarock et al., 2008), initialized using the Pennsylvania State University Ensemble Kalman Filter (PSU-EnKF) system (Zhang et al., 2021). This model will be referred to as the WRF-EnKF simulation and is the Eulerian source model for this study. The other model used is the Ice Crystal Trajectory Growth (ICTG) model (Laurencin et al., 2022).

2.1 Hurricane Harvey Weather Research and Forecasting Ensemble Kalman Filter (WRF-EnKF) Simulation Background

The Hurricane Harvey WRF-EnKF simulation (Zhang et al., 2021) was run using the Weather and Research Forecasting Model version 3.8.1 (Skamarock et al., 2008). The simulation was initialized with data assimilated from all-sky satellite infrared and microwave radiances. The assimilated satellite data consists of all-sky infrared brightness temperatures from channel 8 ($6.2 \mu\text{m}$) of the GOES-16 Advanced Baseline Imager (ABI) and all-sky microwave brightness temperatures ($\sim 19 \text{ GHz}$ and $183.31 \pm 6.6 \text{ GHz}$) from Global Precipitation Measurement (GPM) constellation sensors (Hou et al., 2014; Skofronick-Jackson et al., 2019).

The simulation is configured with four nested domains at horizontal resolutions of 27, 9, 3, and 1 km, with the innermost domain containing 832×832 grid points. It employs the Rapid Radiative Transfer Model for General Circulation Models (RRTMG) radiation scheme for long-wave and short-wave radiation (Iacono et al., 2008). It uses the Thompson microphysics scheme (Thompson et al., 2008). Ensemble Kalman Filter (EnKF) cycling begins at 1200 UTC on 22 August 2017 and is performed hourly through 1200 UTC on 24 August 2017. The simulation is initialized at 0000 UTC on August 24 and produces output every 5 minutes starting at 18z on August 24. Variables extracted from this simulation and used by the ICTG model include winds, temperature, specific humidity, and reflectivity. Figure 2.1 shows the track and intensity of the simulated storm. At the time of the analysis for this study (0400 UTC 25 August 2017), Hurricane Harvey is a Category 1 hurricane with a minimum pressure of 980 hPa and maximum winds of 40 m/s.

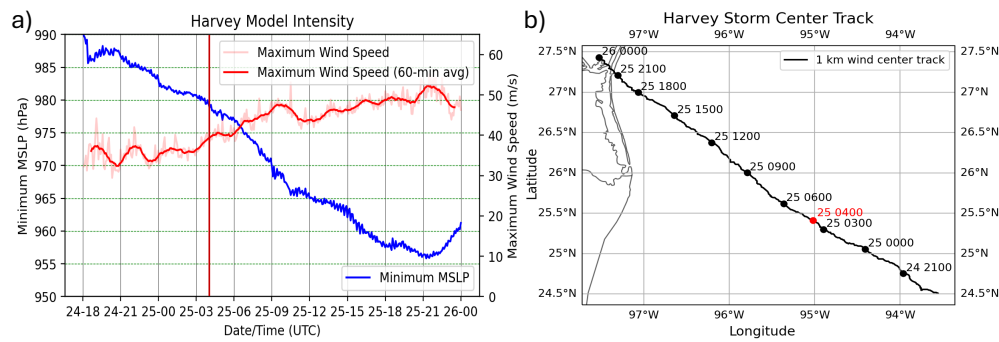


Figure 2.1. Model intensity (a) depicts maximum wind speed in light red, 60-minute average of maximum wind speed in dark red, and minimum sea level pressure in blue. The vertical red line marks the time of analysis- 0400 UTC 25 August 2017. Model Storm Center Track (b) uses 1km wind center tracks marked at every 3 hours. The red point denotes the time of analysis.

2.2 Ice Crystal Trajectory Growth (ICTG) Model Background

The ICTG model, first developed by Laurencin et al. (2022), uses a Lagrangian approach, providing individual crystal tracking. It is run offline separately from the WRF model and operates solely on a single time frame at a steady state. Therefore, the updated crystal information at each time step does not feed back into the source model. The Lagrangian approach provides a more detailed and explicit representation of the wide variety of ice crystals and their growth properties and processes. The model grows and advects individual ice crystals and tracks the evolving ice crystal properties for individual crystals. Additionally, the model calculates the properties of the ice crystals (e.g. axis lengths, effective density, and fall speed) at each time step. The ICTG model uses lab-based parameterizations for crystal growth by vapor deposition (Zhang and Harrington, 2014; Harrington et al., 2019) and riming (Jensen and Harrington, 2015) that account for adaptive habit behavior. The model represents columnar crystals as prolate spheroids and plate-like crystals as oblate spheroids. Melting, aggregation, and secondary ice production (e.g., rime splintering and collision fragmentation) are not accounted for in the ICTG model.

The ICTG model was first used on a quasi-idealized simulation of a leading-convective trailing-stratiform squall line in Oklahoma on 19 June 2007 by Laurencin et al. (2022). The ICTG model effectively simulated realistic crystal growth patterns and paths, accurately representing how individual crystals evolved within the squall line, particularly when varying their initial sizes. Figure 2.2 shows results from Laurencin et al. (2022) where the ICTG model is run with crystals initialized at sizes from 0.04 to 1 mm diameter within the simulated convective tower. A variety of crystal pathways are presented here. The time series of five representative trajectories is shown in Figure 2.2e-i. The location of the crystals with respect to the vertical velocity (Figure 2.2a-d) can affect the speed with which increases or decreases in crystal size occur. Generally, the initially smaller sized crystals are lofted higher within the convective line and are advected rearward to the trailing stratiform region. The initially larger sized crystals quickly fall to the melting level within an hour of initialization. These crystals are too large to stay lofted by the convective updraft.

Overall, Laurencin et al. (2022) found that final crystal sizes and aspect ratios vary

considerably based on a given trajectory. Crystals that remain lofted in a mesoscale updraft tend to grow larger, become more planar, and have an oblate aspect ratio evolution. In contrast, crystals that fall through subsaturated regions undergo sublimation and remain smaller, shrinking from their initial size. Additionally, crystal size sorting is important in generating the reflectivity appearance and structure of a squall line. These differences highlight the importance of both initial crystal size and environmental conditions along each trajectory in shaping the evolution of overall properties of ice crystals.

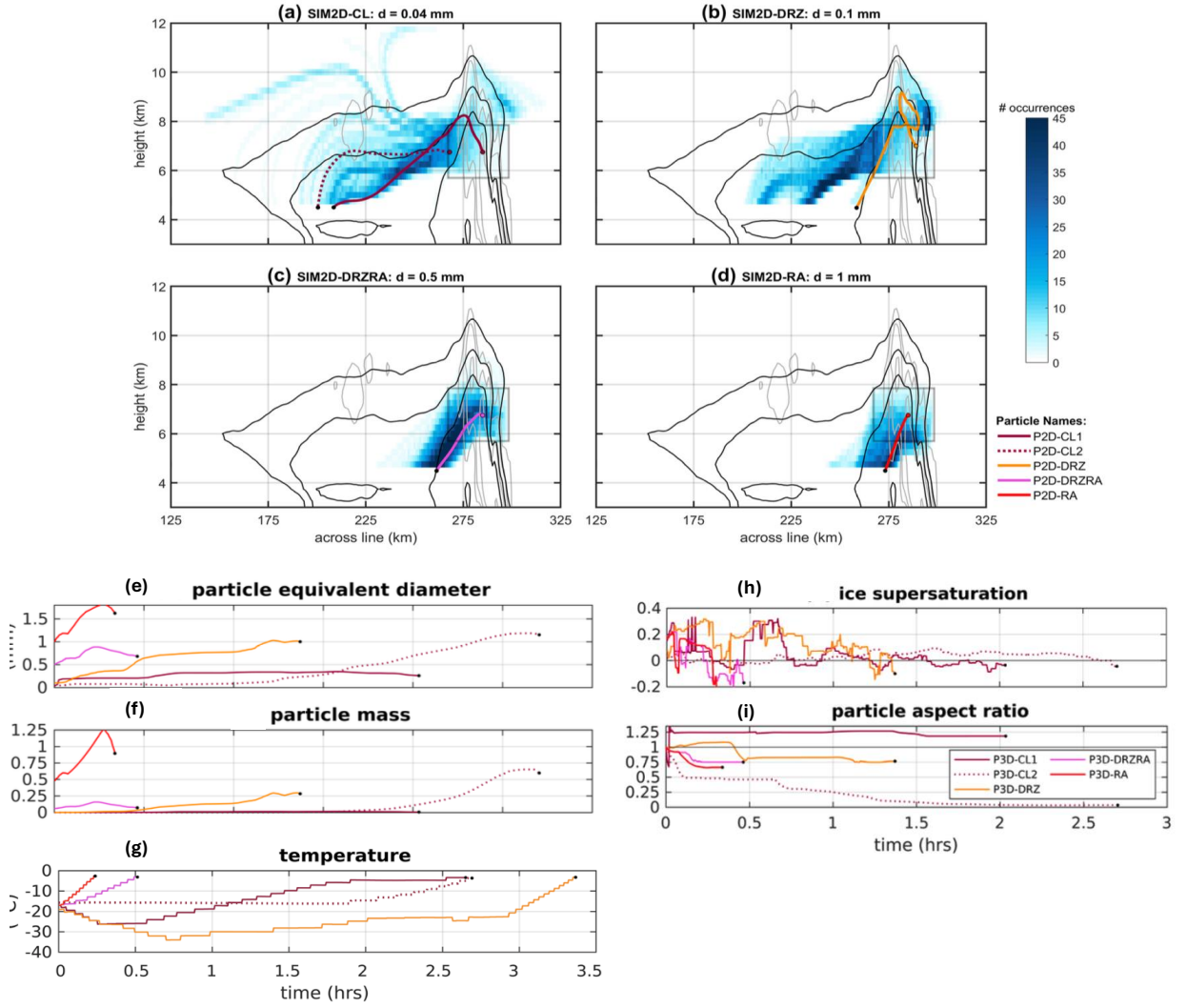


Figure 2.2. Figure adapted from Laurencin et al. (2022) Figures 5 and 6. Ice crystal trajectories are simulated within a leading-convective trailing-stratiform squall line. Crystals are initialized within the gray square, trajectory density is shaded, and reflectivity and vertical velocity are contoured (a-d). Time series of crystal properties shown in e-i

2.3 Ice Crystal Initialization and Model Integration

While Laurencin et al. (2022) initializes crystals within a grid box at set sizes for each grid point, this study uses an updated initialization method developed by Rojas et al. (2025). Overall, this is an approach that is more dependent on the source model microphysics,

ensuring that the initialization location and sizes are more consistent with the WRF-EnKF microphysics output. In the ICTG model, initialization grid boxes must have the following characteristics: (1) Ice mixing ratio > 0 , (2) Ice number concentration > 0 , and (3a) Cloud ice concentration tendency from cloud water freezing > 0 OR (3b) cloud ice concentration tendency from rainwater freezing > 0 . Additionally, all crystals must initially be located within the eyewall (defined as < 40 km from the calculated center of the TC) as this study focuses specifically on TC eyewall microphysics. The crystals are initialized as isometric (aspect ratio of 1), on a 3 km by 3 km grid horizontally, and at every 1 km vertically from 6 km to 12 km altitude. This analysis investigates the evolution of modeled ice crystals in Hurricane Harvey (2017) at 0400 UTC 25 August 2017.

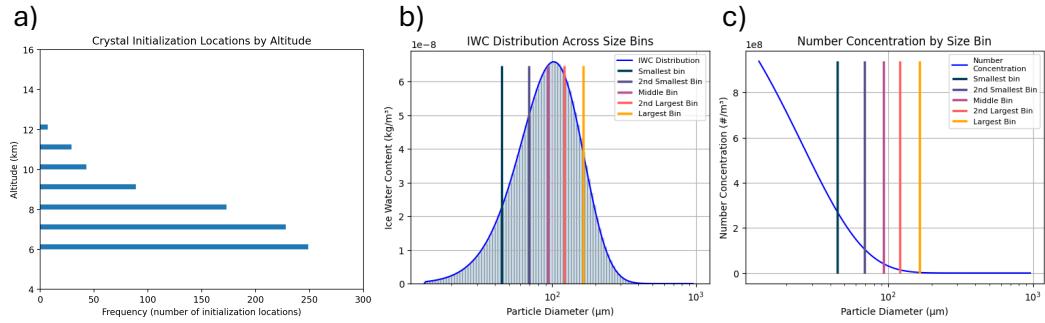


Figure 2.3. Frequency distribution of crystal initialization locations by altitude (a). 818 locations selected for crystal initialization based on noted criteria. (b) IWC Distribution and (c) Number Concentration by Size Bin displays the source model microphysical information for a single initialization location. Vertical colored lines in (b) and (c) show the 5 selected crystal initial sizes based on the IWC percentiles.

Overall, 818 initialization grid boxes meet the criteria defined above and are shown in Figure 2.4a. Figure 2.3a shows that generally more crystals are initialized at lower levels above the melting level (6-8 km), but there are still numerous crystals that initialize between 9 and 12 km. These areas align closely with where the formation of new ice crystals would be expected. The number of initialization locations decreases strongly with altitude due to the altitude-dependent initialization criteria. This dependence arises because moisture decreases with altitude. As you go higher in the atmosphere, more liquid water has already frozen at lower levels, leaving less liquid water available to freeze, which reduces the likelihood of new ice crystal formation.

Five different crystal sizes are initialized at each of the 818 initialization grid boxes. Therefore, there are 4090 individual crystals are initialized. The five sizes are determined by first calculating the particle size distribution (PSD) at each grid box within the

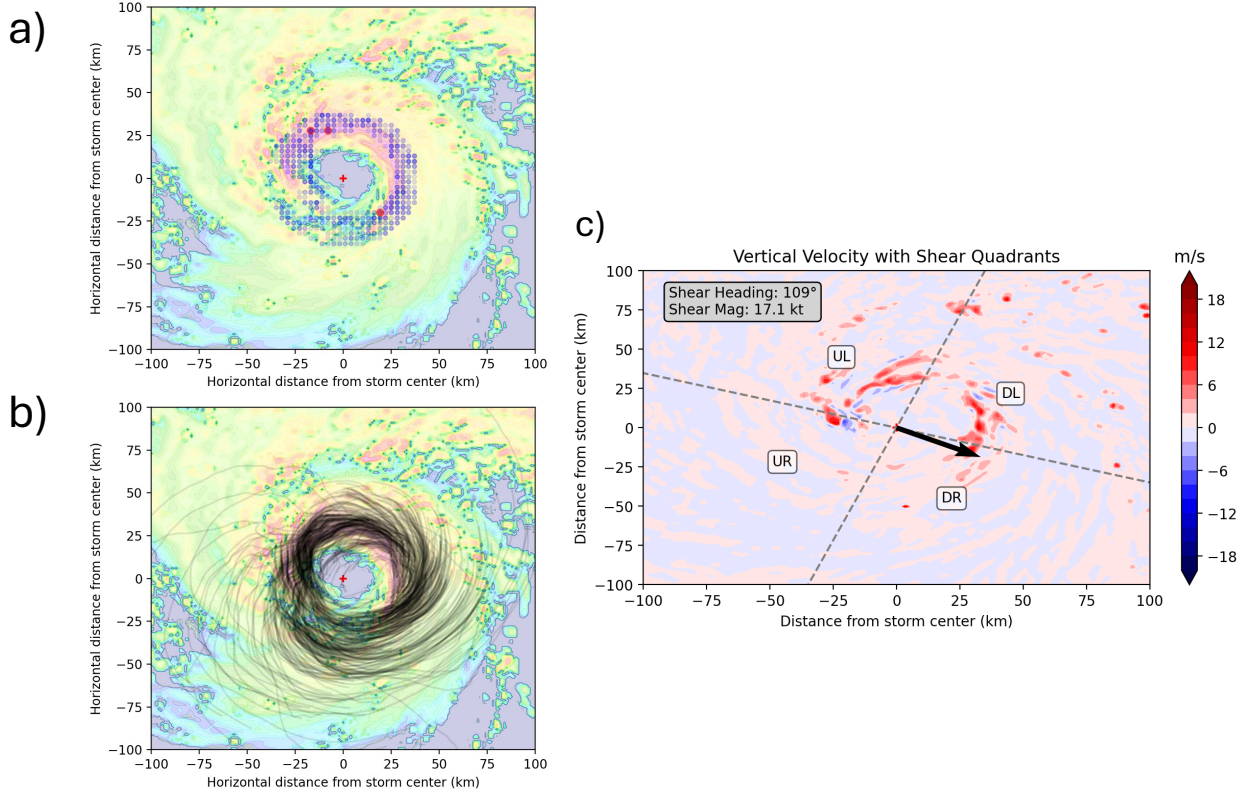


Figure 2.4. Simulated Radar Reflectivity Plan Views for Hurricane Harvey at 2 km altitude. All crystals are initialized at blue dots (a). Crystals analyzed here are initialized at red dots (a). All crystal trajectories for the middle size bin at each initialization location (b). Vertical Velocity Plan View for Hurricane Harvey at 6 km altitude (c) with shear quadrants and shear heading denoted.

WRF-EnKF model. The Thompson Aerosol microphysics scheme, used in WRF-EnKF, uses a gamma PSD assumption. The initial crystal sizes depend on PSDs and ice water content (IWC) and are based on the following equations:

$$N_{\text{ice}} = Q_{\text{nice}} * \rho_{\text{air}} \quad (2.1)$$

$$PSD = N_{\text{ice}} \lambda_{\text{ice}} e^{(-\lambda_{\text{ice}} D)} \quad (2.2)$$

$$\text{IWC} = \int_{D_{\min}}^{D_{\max}} D^3 \frac{\pi}{6} \rho_i N_0 e^{(-\lambda D)} dD \quad (2.3)$$

where N_{ice} is the number concentration of ice particles per cubic meter, Q_{nice} is the number mixing ratio (number per kilogram of air), ρ_{air} is the air density, N_0 and λ are the

intercept and slope parameter of the particle size distribution (PSD) from the microphysics scheme, D is the ice crystal diameter, ρ_{ice} is the density of ice, and $\rho_i = 890 \text{ kg m}^{-3}$ is the density of ice as prescribed for the ice crystal category in the Thompson microphysics scheme. The bounds of the integral are the minimum and maximum diameter. Figure 2.3b and Figure 2.3c show these IWC distribution and PSD calculations.

Next, the 5 initial chosen crystal sizes are the 10th, 30th, 50th, 70th, and 90th percentiles of IWC at each initialization grid box location (Figure 2.3b). This allows us to capture a wide range of feasible possible crystal sizes. When looking at the number concentration by size distribution in Figure 2.3c, it is shown that these crystals are generally on the larger end of the spectrum. However, we sample the IWC curve evenly so that the selected sizes are a good representation of the ice mass within a particular grid box.

The ICTG model is integrated for 8 hours and outputs data at 20-second intervals. The ICTG model outputs exact location data at each time step allowing us to plot the trajectories of each individual crystal. A subset of crystal trajectories is shown in Figure 2.4b. Additionally, the ICTG model outputs crystal data and environmental data, including temperature, ice supersaturation, accumulated rime mass, mass, vertical velocity, and the a and c diameters of the simulated spheroid. The a and c dimensions are used to calculate the aspect ratio ($\theta = \frac{c}{a}$). When $\theta > 1$, crystals are considered columnar and when $\theta < 1$, crystals are considered planar. The aspect ratio is fixed when temperatures are below -30°C due to a limitation within the ICTG model. Azimuthal positions and radial positions are calculated from the outputted data.

The outputted crystal property data was analyzed to select certain unique and extreme ice crystals and further analyze their behavior and potential causes for their behavior. These categories are listed below:

Extreme	Unique
Largest Mass	Sublimation in Eye
Longest Lasting	1 or more Revolutions
Lowest Aspect Ratio	Radially and Azimuthally Cycling
Furthest Final Radial Distance	

Table 2.1. Extreme and Unique Crystal Categories identified and analyzed in this study

Chapter 3

Results

Table 3.1 lists the ice crystals to be examined in this section. The table notes the ice crystal's given name based on our analyses, size bin, unique/extreme characteristic(s), initial mass (in mg), and which figure(s) each ice crystal appears in. These crystals span a range of initial sizes and will enable a comprehensive assessment of their dynamic behavior, varied trajectory paths, and differing ice crystal properties within a TC.

Crystal Name	Unique/Extreme Characteristic(s)	Size Bin	Initial Mass (mg)	Shown in Figure(s)
FC1 (Crystal 1)	Largest Mass; Lowest Aspect Ratio	1	3.18×10^{-5}	3.1–3.3
FC2 (Crystal 2)	Largest Mass; Lowest Aspect Ratio	2	1.17×10^{-4}	3.1–3.3
FC3 (Crystal 9)	One or More Revolutions	5	1.08×10^{-3}	3.4–3.7
FC4	Furthest Radial Distance; Longest-Lasting	1	4.13×10^{-5}	3.8–3.11
FC5	Sublimation within Eye	2	1.52×10^{-4}	3.8–3.10, 3.12
FC6	Radial and Azimuthal Looping	3	3.33×10^{-4}	3.8–3.10, 3.13
AC1		4	1.59×10^{-3}	3.2–3.3
AC2		3	1.73×10^{-4}	3.5–3.7
AC3		4	3.79×10^{-4}	3.5–3.7
Crystal 3	Largest Mass	1	1.07×10^{-6}	3.1
Crystal 4	Largest Mass	2	1.34×10^{-6}	3.1
Crystal 5	Largest Mass	4	7.29×10^{-4}	3.1
Crystal 6	Lowest Aspect Ratio	1	3.18×10^{-5}	3.1
Crystal 7	Lowest Aspect Ratio	5	1.23×10^{-3}	3.1
Crystal 8	Lowest Aspect Ratio	4	1.07×10^{-6}	3.1
Crystal 10	One or More Revolutions	4	5.61×10^{-4}	3.4
Crystal 11	One or More Revolutions	3	2.92×10^{-4}	3.4
Crystal 12	One or More Revolutions	5	1.23×10^{-3}	3.4
Crystal 13	One or More Revolutions	2	1.03×10^{-4}	3.4
Crystal 14	Sublimation within Eye	12	1.34×10^{-4}	3.14–3.16
Crystal 15	Large Azimuthal Distance	18	2.56×10^{-4}	3.14–3.16
Crystal 16	Sublimation within Eye	20	2.92×10^{-4}	3.14–3.16

Table 3.1. Unique/Extreme Characteristic(s), size bin, initial mass (in mg), and figure references for selected crystals.

3.1 Extreme Crystals- Largest Mass and Lowest Aspect Ratio

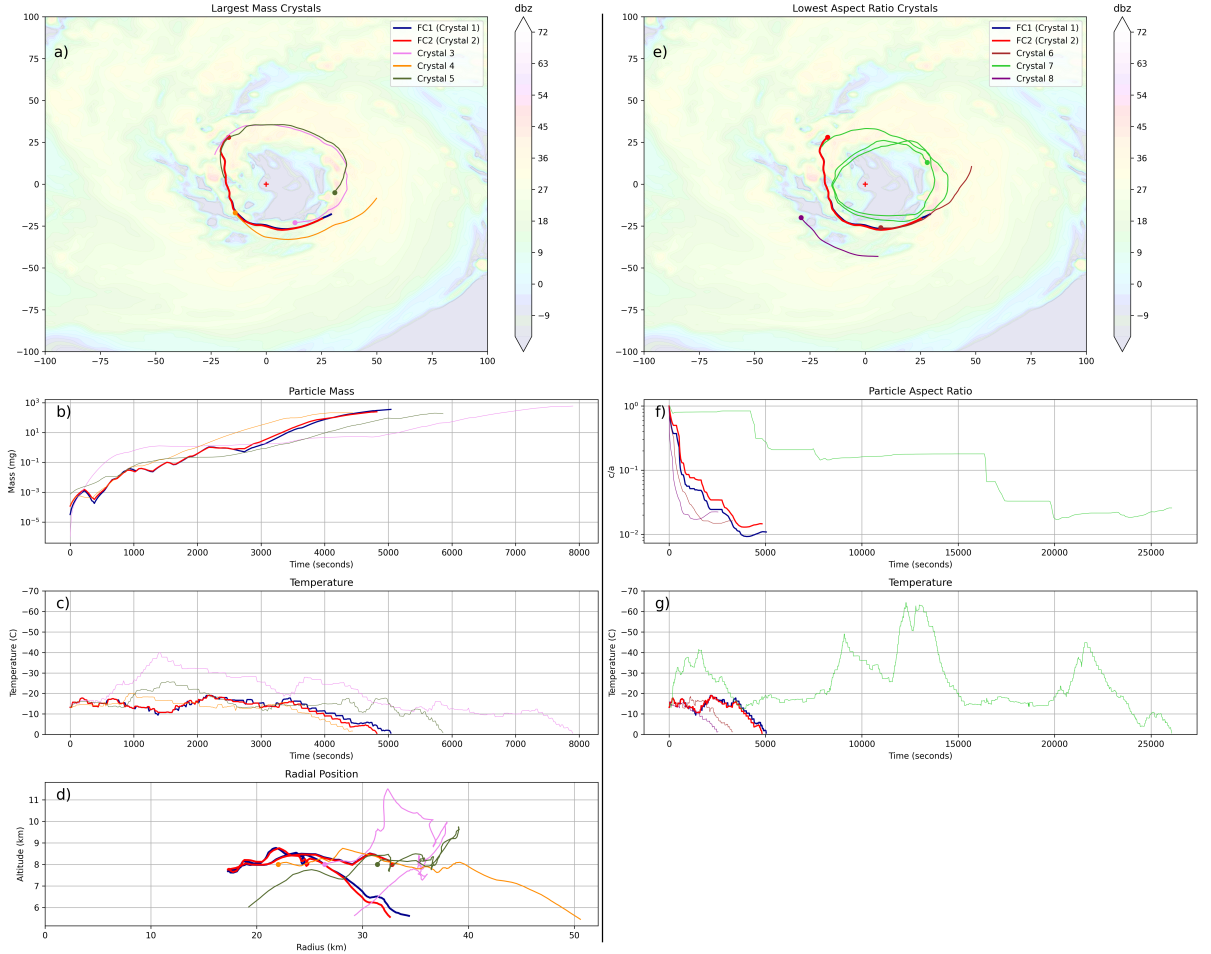


Figure 3.1. Crystals are initialized at the dots. Colored trajectories denote different extreme crystals that meet the specified criteria- largest mass crystals in (a), (b), (c), and (d) and lowest aspect ratio crystals in (e), (f), and (g). Reflectivity in (a) and (e) at 6.5 km altitude.

First, the analysis will focus on the crystals that attain extreme values in both mass and aspect ratio. The crystals with the largest mass have likely attained this extreme size through extreme dendritic growth, which directly corresponds to an extremely low aspect ratios (modeled as oblate spheroids). Figure 3.1 shows the crystal trajectories with the five largest masses and the five lowest aspect ratios out of the 4090 crystals initialized in

the simulation. Regarding the five largest mass crystals seen in Figure 3.1a-d, all five initialize at 8 km altitude. These crystals range in initial size from 1.17×10^{-6} mg to 7.29×10^{-4} mg. Additionally, Figure 3.1d shows that all five crystals initialize at different locations within the TC eyewall, but follow somewhat similar growth patterns as seen in Figure 3.1b. Each crystal has relatively steady growth until the end of their lifetimes when each of them experiences extreme mass growth. This is due to being located within the dendritic growth zone (DGZ) for much of their lifetimes (Figure 3.1c). The DGZ allows efficient crystal growth via vapor deposition. Regarding the bottom five lowest aspect ratio crystals seen in Figure 3.1e-g, all five quickly become plate-like crystals as indicated by their particle aspect ratio being less than one (Figure 3.1f). Four of these five crystals (Crystals 1, 2, 6, and 8) only survive for less than 5000 seconds. These four crystals all experience rapid drops in their aspect ratios and quickly fall to the melting level as seen in Figure 3.1g. The fifth crystal (Crystal 7 in Figure 3.1e-g) differs from the other four crystals. It lasts until nearly the end of the simulation and completes over 2 revolutions around the storm. This crystal has several rapid rises and drops in temperature and numerous subsequent drops in its aspect ratio until it reaches a bottom five lowest aspect ratio for this simulation. The extreme categories, including highest mass and lowest aspect ratio, span all azimuthal locations and initial sizes, yet Crystals 1 and 2 initialize at the same location, have similar trajectories, and are present in both categories.

The two focus crystals- now referred to as FC1 (blue) and FC2 (red) in Figure 3.2 at size bins 1 and 2 at this location- achieve both a top five highest mass and a bottom five lowest aspect ratio. The mean maximum mass for each crystal, calculated across all 4090 crystals, is 1.95 mg, while the mean aspect ratio is 1.18. Roughly 25 crystals that initialize near the same location as FC1 and FC2 grow to a mass exceeding 0.1 mg. We will further analyze FC1 and FC2 in more detail in the following paragraphs and compare these crystals to other crystals with similar initial sizes and locations. This comparison allows us to understand how sensitive initial size and/or initial location are to the overall trajectory outcome. Overall, the region of the eyewall where these crystals initialized exhibited typical updraft conditions, which led to a wide range of trajectory outcomes, yet still produced two of the largest crystals in the entire simulation.

As previously noted, FC1 and FC2 both initialize at the same location with similar sizes and have generally similar trajectories. Figure 3.2 shows their crystal evolutions in detail, along with other trajectories explained in the next paragraph. FC1 and FC2 come from size bins 1 and 2 and thus are the two smallest initial sizes of the five crystals

initialized at that location. These two crystals end with the largest final masses of these five crystals. The smallest initial crystal of the five, FC1, initializes with a diameter of 0.041 mm, mass of 3.18×10^{-5} mg, and ends as the largest crystal of the five at 356.57 mg. This crystal reaches the second heaviest final mass of the 4090 individual crystals within this ICTG simulation. FC2 initializes with a diameter of 0.063 mm, mass of 1.17×10^{-4} mg, and achieves a final mass of 245.81 mg. FC1 and FC2 are located within the DGZ for much of their lifetimes (Figure 3.2b). The DGZ allows efficient crystal growth via vapor deposition and is favorable for plate-like growth. The fastest growth of these two crystals occurs between 2000 and 4000 seconds (Figure 3.2f) when both crystals are firmly located in the DGZ. Ice supersaturation (Figure 3.2c) remains above zero for a significant duration of FC1 and FC2's lifetimes. When the ice supersaturation is greater than zero, crystal growth is favored. From around 3000 seconds until the crystals reach the melting level, there is significant growth of both crystals seen by the corresponding increase in their masses (Figure 3.2f). The two crystals sink to the melting level relatively quickly and melt. Figure 3.2g shows that there is a rapid decrease in the aspect ratios of FC1 and FC2 immediately after initialization until 1500 seconds. A steady decrease in the aspect ratios continues for both crystals until they reach the melting level.

To understand what makes these focus crystals so unique among the typical background setup, we will focus on the two focus crystals and variations of those crystals, including varying initial size and spatial variations of initial locations. Crystals that are not singled out for detailed analysis at each initialization location will be referred to as alternate initial size crystals (ACs). Figure 3.2 focuses on FC1, FC2, and the largest alternate initial size crystal at that location (AC1), which is located at Size Bin 5. We can now compare how a larger initial crystal with the same initial location (AC1) behaves in comparison to the other smaller initial crystals (FC1 and FC2) at that location. This will illustrate the sensitivities of the crystals to the initial size. Other crystal trajectories are also shown to illustrate the sensitivity of the crystals to their initial location. These are referred to as spatially adjacent crystals (SACs) and are initialized within 45° azimuth of the focused initialization location, initialized at the same altitude level as the FCs or within ± 1 km altitude, and initialized at the same size bins as the FCs. Therefore, the SACs are only located at size bins 1 and 2 in Figure 3.2. The 45° azimuth range around the focused initialization location was chosen to ensure a representative spatial sampling.

AC1 initializes with a mass of 1.59×10^{-3} mg. Within the first 2000 seconds, we see in Figure 3.2 that AC1 begins to develop characteristics that differ from FC1 and FC2.

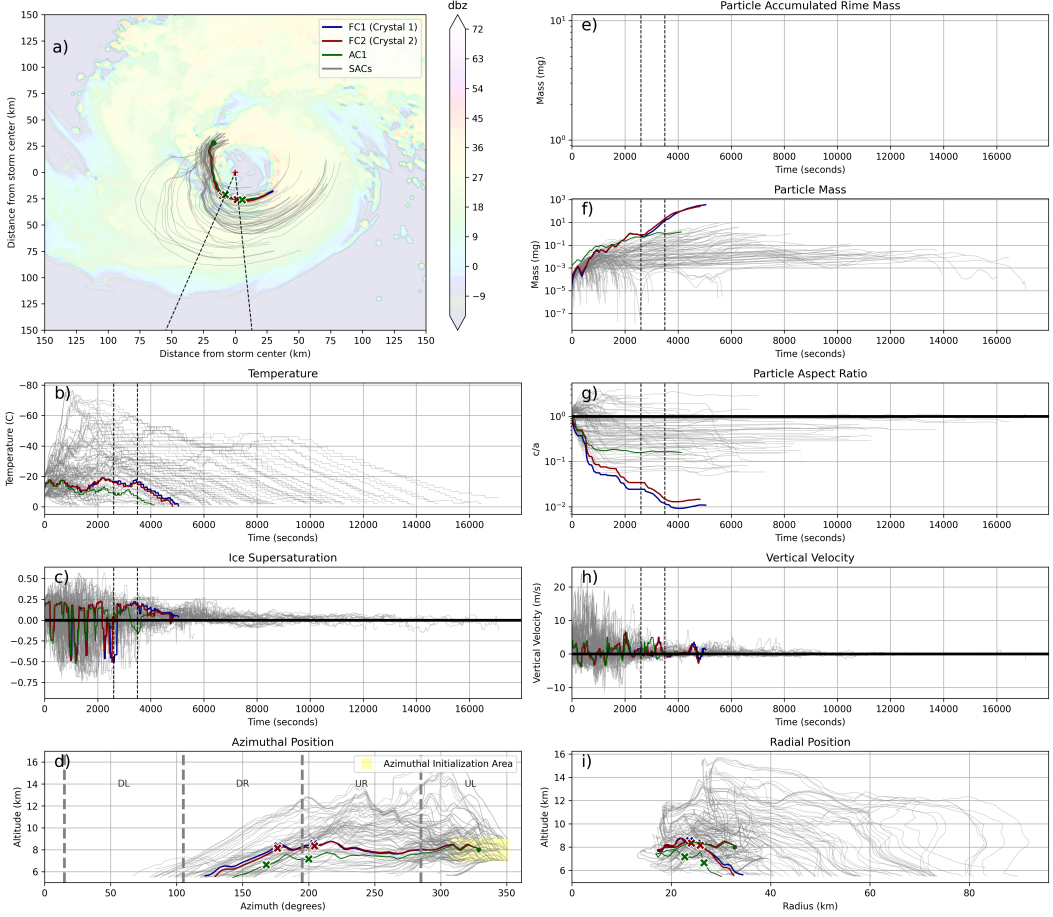


Figure 3.2. Crystals are initialized at the dot. Colored trajectories denote different initial size bins. Gray trajectories are other crystals initialized within the yellow box (d). Reflectivity in (a) at 6.5 km altitude. Shear quadrants are marked in (d). Black dashed lines and colored markers denote 2600 seconds and 3500 seconds when further analysis occurs.

In the first 1000 seconds, AC1 remains within the DGZ along with FC1 and FC2, but then falls into slightly warmer temperatures (Figure 3.2b) due to its heavier mass seen in Figure 3.2f. AC1 is then located at slightly warmer temperatures than the DGZ for much of the rest of its lifetime. It still has similar ice supersaturation during this time, and continues to grow, but its aspect ratio stalls and remains higher than FC1 and FC2 (Figure 3.2g). This is due to the combination of the higher temperatures and the larger mass. A crystal that is larger in size requires more deposition growth in order to alter the aspect ratio. FC1 and FC2 are smaller and thus it is easier for them to become more oblate more rapidly (Sheridan et al., 2009). After 2000 seconds, it is clear that the impact of the larger initial size means that AC1 remains continuously below the DGZ in Figure

3.2b, thus experiencing drier and lower supersaturation air seen in Figure 3.2c. This leads to a much slower growth rate and ultimately a smaller and less oblate crystal than FC1 and FC2. With respect to the final aspect ratio of these crystals, FC1 and FC2 have by far the lowest and most extreme aspect ratios (Figure 3.2g). More specific time steps will be further analyzed in later paragraphs.

As noted previously, the SACs all initialize within the eyewall region (defined as < 40 km from the calculated center of the hurricane), yet numerous SACs deviate outside of this region as the simulation progresses. SACs reach as far as 90 km away from the center of the TC (Figure 3.2i). Both of the focus crystals are located within the eyewall (15-35 km radially) as well as the downshear-left, downshear-right, and upshear-right eyewall regions of Hurricane Harvey for their entire lifetimes (Figure 3.2d and Figure 3.2i). The SACs are generally lofted relatively quickly following initialization (Figure 3.2h) and are then located higher within the storm (Figure 3.2d) and further from the eye (Figure 3.2i). Consequently, these crystals experience slower growth due to their location within regions of lower moisture present at the higher altitudes. The SACs that initialize at higher altitudes are more easily lofted out of the DGZ and further away from the eyewall. Therefore, they do not grow as much as FC1 and FC2 do as the SACs are located in less favorable growth zones. The SACs that initialize at lower altitudes are located beneath the DGZ at initialization, so they're prone to grow more slowly and fall out more quickly.

In order to better understand the particular behavior of these crystals, the kinematic and thermodynamic fields were further investigated. Specifically, two time steps within the simulation were scrutinized to better understand the relationship between the trajectories and the kinematic and thermodynamic fields: 2600 seconds (200° azimuth) and 3500 seconds (175° azimuth). Figure 3.3 shows radial cross sections of ice supersaturation and vertical velocity and an azimuthal cross section of vertical velocity. Overall, there are large fluctuations in the ice supersaturation and large differences in mass at 2600 seconds and 3500 seconds between FC1, FC2, and AC1.

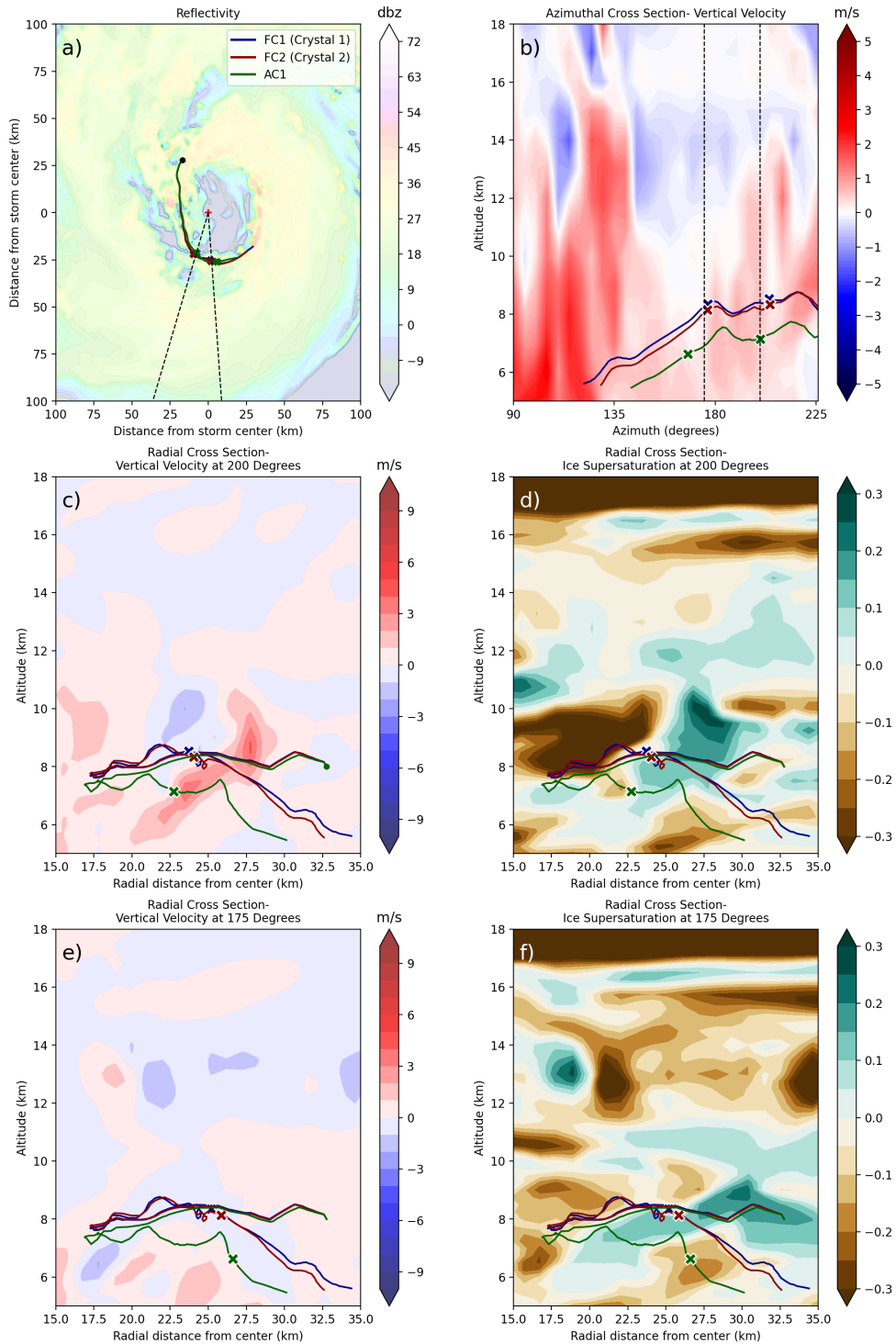


Figure 3.3. Crystals are initialized at the black dot in (a). Colored trajectories denote different initial size bins. Reflectivity in (a) at 6.5 km altitude. Azimuthal cross section (b) with vertical velocity radially averaged between 15 km and 35 km radius. Radial cross sections along dashed lines in (a and b) at 200° azimuth (c and d) and 175° azimuth (e and f).

Throughout their lifetimes, FC1 and FC2 closely overlap with each other. As they approach 200° azimuth (2600 seconds), in Figure 3.2f, it is shown that both crystals lose mass due to moving through a region of low ice supersaturation. This region is associated with a decrease in the strength of updraft that is present and dry eye air at this location. At 2600 seconds as seen in Figure 3.2c, ice supersaturation for FC1 and FC2 is nearly zero. AC1 is located within a region of positive ice supersaturation values at this time (Figure 3.3d). The crystal is able to sustain its mass more than the other crystals (Figure 3.2f). Additionally, all three crystals are moving into regions of higher vertical velocity (Figure 3.3c). A corresponding slight increase in altitude is seen as these crystals progress through time.

Between 200° azimuth (2600 seconds) and 175° azimuth (3500 seconds), the three crystals have differing mass behaviors as seen in Figure 3.2f. The mass growth of AC1 stalls as it moves into a region of lower ice supersaturation (Figure 3.3f). Mass growth rapidly occurs for FC1 and FC2 as these crystals move into a more favorable growth environment where ice supersaturation is more positive (Figure 3.3f). Generally, these crystals are moving through regions of positive vertical velocity shown in Figure 3.3b. At 3500 seconds, AC1 has the lowest ice supersaturation of the three crystals. It is clearly located in a drier region than the other two crystals (Figures 3.2c and 3.3f). Figure 3.2f shows that the mass growth of this crystal is negligible with little to no change in the mass. FC1 and FC2 continue to grow rather quickly due to their location within regions of positive ice supersaturation and the DGZ (Figures 3.2b, 3.2f and 3.3f). Following this time step, FC1 and FC2 are quite large and heavy crystals, so they begin sinking towards the melting level. AC1, which was already smaller than FC1 and FC2 at this point in time, also sinks towards the melting level. Overall, we found that FC1 and FC2 were quite extreme because they remained within the DGZ for much of their lifetimes, promoting rapid plate-like growth. Their large size also allowed them to survive interactions with dry air and they stayed within the eyewall region throughout their lifetimes, which is a favorable region for rapid growth due to presence of areas of strong vertical velocity.

3.2 Unique Crystals- One or More Revolutions

As previously demonstrated, eyewall updrafts are able to affect ice crystal characteristics and cause them to behave differently as a result. Here, we will examine long-revolving ice crystals to help identify potential regions where Eulerian microphysics scheme

assumptions could break down. The eyewall is known to be a region with limited amounts of supercooled water. It is hypothesized that this is due to the long residence times of ice crystals within the eyewall and the constant upwind seeding of ice crystals (Cecil and Zipser, 2002; Black and Hallett, 1999). As a result, we want to analyze crystals with long eyewall residence times, such as those that complete more than one revolution around the TC. Furthermore, the strong horizontal winds and wind shear within a TC promote complex mixing of the precipitating particles, resulting in diverse trajectories and variations in crystal properties.

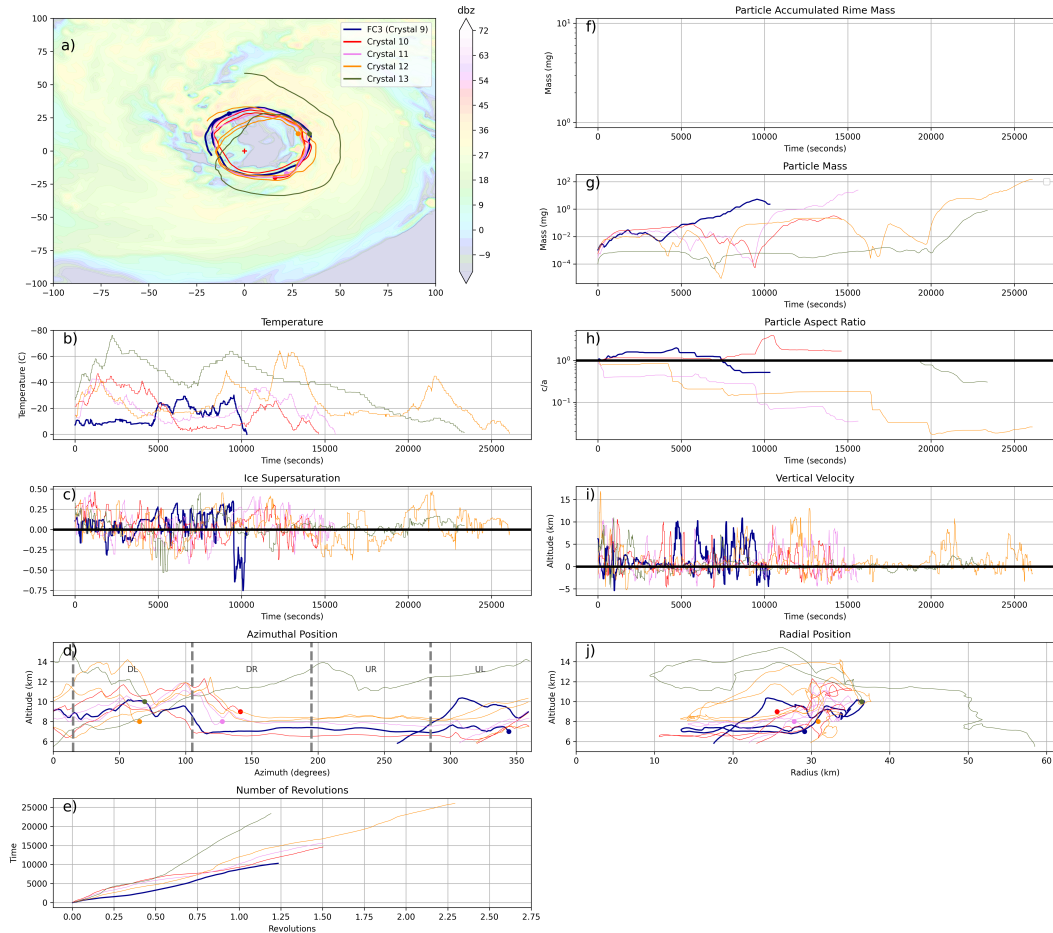


Figure 3.4. Crystals are initialized at the dots. Colored trajectories denote different extreme crystals that meet the specified criteria. Reflectivity in (a) at 6.5 km altitude. Shear quadrants are marked in (d).

Figure 3.4 shows the five longest-revolving crystals within the simulation: FC3 (Crystal 9), which completes nearly 1.25 revolutions around the TC; and four additional

crystals, Crystals 10-13, which also complete at least one revolution around the TC. In total, only 14 ice crystals out of the 4090 individual crystals complete at least one revolution around the TC. Crystals 10-13 in Figure 3.4 initialize between 8 and 10 km altitude at varying azimuths between 60° and 150° azimuth (Figure 3.4d). Figure 3.4g demonstrates that their initial sizes range from 1.03×10^{-4} mg to 1.23×10^{-3} mg. Figure 3.4e shows the revolution distance compared to the time since initialization. This is a way to visualize the amount of time it takes for each crystal to complete a revolution around the TC. For example, Crystal 13 is moving at the fastest "azimuthal" speed, while FC3 is moving at the slowest "azimuthal" speed out of these five crystals.

After initialization, the azimuthal position plot, Figure 3.4d, shows that the four crystals, except for Crystal 13, traverse the TC in very similar manners. Between 150° and 300° azimuth, the four crystals are advected between 6 and 9 km altitude. In the other azimuths, there is no clear pattern present between these crystals. Figure 3.4i displays the two distinct phases of these crystals. Regions where more active updrafts of the storm are located are regions where the crystal experiences stronger vertical velocity. These are the downshear-left and upshear-left regions as seen in Figure 3.4d. In these regions, updrafts are actively lofting the crystals to higher altitudes at azimuths outside of the 150° to 300° azimuth region. In the 150° to 300° azimuth region, there are fewer updrafts, which allows strong tangential winds to move the crystals along at relatively steady altitudes. These different updraft regions are a result of the wavenumber-1 asymmetry of vertical velocity that develops due to the environmental wind shear (e.g., Rojas et al. (2024)). The locations of strong updrafts and the wavenumber-1 asymmetry are very typical of single eyewall TCs when they interact with environmental wind shear. Environmental wind shear causes vortex tilt and differential vorticity advection, which act to strengthen updrafts in the downshear quadrants. The dominant influence on the eyewall structure shifts to direct shear effects as the TC evolves, resulting in an upwind shift in updraft and reflectivity maxima seen in this simulation (Bender, 1997; Frank and Ritchie, 1999). This phenomenon was further analyzed in Rojas et al. (2024); Didlake et al. (2017, 2018); DeHart et al. (2014); Jones (1995); Corbosiero and Molinari (2002), and Corbosiero and Molinari (2003).

FC3 is initialized in the upshear-left quadrant and is located within the DGZ for the first 4000 seconds allowing for rapid growth until some slight mass loss due to reaching colder temperatures (Figure 3.4b and Figure 3.4g). FC3 then moves through several updrafts and regions of positive vertical velocity (seen in Figure 3.4i) leading to rapid

growth until it grows quite large and falls to the melting level. FC3 maintains columnar growth until a decrease in ice supersaturation around 9000 seconds (Figure 3.4c) causes the crystal to transition to more plate-like growth (Figure 3.4h). Figure 3.4g shows that Crystals 10-12 follow similar mass patterns to each other. As seen in Figure 3.4h, Crystals 11 and 12 have plate-like growth throughout their lifetimes, while Crystal 10 is nearly isometric until a transition to columnar growth near the end of its lifetime. All three crystals grow rather quickly and then enter areas of lower vertical velocity causing a loss in mass. The crystals each pass through several updrafts within the downshear-left and upshear-left regions allowing for growth of the crystals to resume. All three crystals eventually reach the melting level (Figure 3.4b), with Crystal 12 taking the longest to do so. Additionally, the four crystals, except for Crystal 13, are located within the eyewall at 10 to 35 km radius for their entire lifetimes.

Throughout its lifetime, Crystal 13's behavior greatly differs from Crystals 9-12. Figure 3.4d shows that it is initialized at the highest altitude of these five crystals. This causes it to grow at a slower rate than the other four crystals and maintain a lower mass (Figure 3.4g). It stays between 12 and 15 km altitude for much of its lifetime and is ejected to a larger radius than the other four crystals as a result (Figure 3.4j). Overall, throughout its lifetime, it is generally located at higher altitudes and lower temperatures than Crystals 9-12 (Figure 3.4b). Crystal 13 takes nearly 25,000 seconds to complete the 1.25 revolutions that the blue crystal completes in approximately 10,000 seconds — a much longer amount of time. Overall, Crystal 13 appears to be an outlier in comparison to the four other crystals.

The analysis now focuses on FC3 and crystals that initialize at the same location as FC3 (AC2 and AC3), which is at 7 km altitude and 345° azimuth. It is clear that FC3 is initiated at the tail end of the eyewall updraft region, allowing it to overlap its trajectory more downwind and fall out more downwind than the other crystals in Figure 3.4. Therefore, we chose this unique starting position for a quasi-fixed location analysis as in Figure 3.3 to better understand the sensitivity of initial location, altitude, and/or size to the evolution of similar crystals. AC2 and AC3 are located at smaller initial size bins than FC3. It is important to note that FC3 is initialized at the largest size bin at this location and has an initial mass of 1.08×10^{-3} mg. After 2500 seconds, FC3 has the smallest mass out of the three crystals at 1.79×10^{-2} mg (Figure 3.5f). The ACs reach the DGZ relatively quickly — between 1000 and 2500 seconds — allowing them to reach a higher mass (Figure 3.5b and Figure 3.5f) and lower particle aspect ratio (Figure 3.5g)

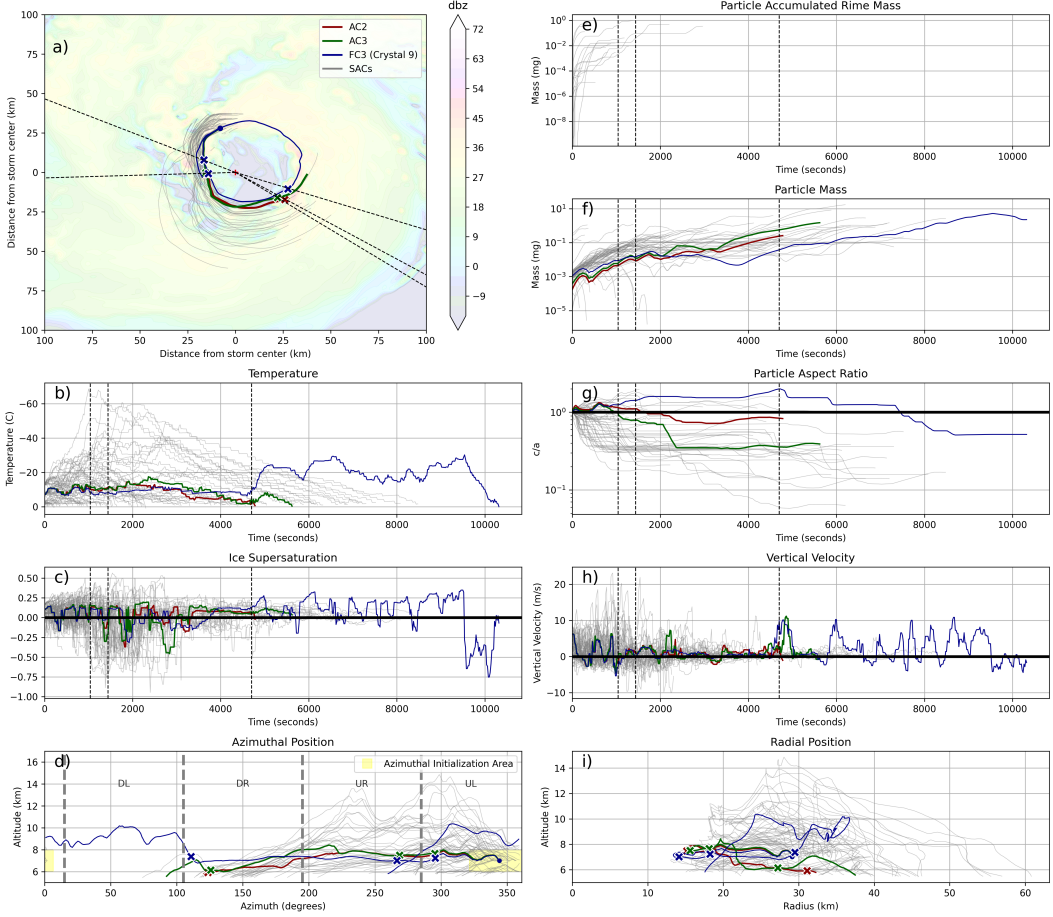


Figure 3.5. As in Figure 3.2 for a different initialization location. Black dashed lines and colored markers denote 1040 seconds, 1440 seconds, and 4700 seconds when further analysis occurs.

than FC3. The ACs cannot stay lofted within the hurricane as a result. Figure 3.5b shows that FC3 is located below the DGZ and within a region of favorable columnar growth (-2° to -8° C) during this time period, causing it to have a higher aspect ratio. As shown in Figure 3.5d and Figure 3.5f, the ACs eventually become too large to stay lofted and fall to the melting level within the downshear-right and downshear-left quadrants between 130° azimuth (4600 seconds) and 90° azimuth (5600 seconds). These crystals also spend a significant amount of time in areas of negative ice supersaturation around 2750 to 4000 seconds (Figure 3.5c), which limits growth during this portion of their lifetimes (Figure 3.5f). Also, we see in Figure 3.5g that the ACs are more plate-like in shape than FC3 is during this period in time. These are considered typical crystal pathways- those crystals that are lofted by an updraft, grow to a large size and start to sink quickly toward the melting level. Meanwhile, FC3 continues to stay relatively steady in mass until it reaches

110° azimuth at 4700 seconds seen in Figure 3.5d and Figure 3.5f.

FC3 initializes in the upshear-left quadrant of the hurricane. Once the crystal approaches the downshear-left quadrant, where updrafts are most favored relative to the shear vector, the crystal is lofted upwards by an updraft (Figure 3.5d and Figure 3.5h) around 110° azimuth. FC3 stays lofted between 7 and 10 km (Figure 3.5d) for the rest of its lifetime and the crystal generally remains within the DGZ aiding in the increase in mass (Figure 3.5b and Figure 3.5f). The crystal is at or above the median mass after 7000 seconds when compared to the ACs and SACs. Note that the overall number of crystals significantly decreases as the simulation continues and the crystals melt or sublime. Furthermore, Figure 3.5d shows that no other ACs or SACs reach the azimuthal position that FC3 does - between 0° and 75° azimuth. This is because the SACs are advected to larger radii than FC3 (Figure 3.5i). At large radii, it takes longer for the crystals to travel azimuthally. Therefore, FC3 completes nearly 1.25 revolutions around the TC in less time than it takes for any SAC to complete 3/4 of a revolution. As seen in Figure 3.5b, the SACs are all sinking toward the melting level after around 6000 seconds.

Additionally, riming mass accumulation is observed exclusively in the SACs. The FC and ACs do not have any riming occurring as shown by Figure 3.5e. It has been observed in Rojas et al. (2025) that only a subset of the crystals initialized at 6 km altitude encounter riming. Supercooled liquid water exists just above the melting level in the updrafts, so any crystals initialized at higher altitudes than 6 km do not fall through the updraft down to the melting level. The crystals instead fall out in regions outside the updraft, and thus fall through the region just above the melting level, where there is no updraft and thus no supercooled liquid water. Meanwhile, the SACs that have riming in this simulation gain rime mass because they fall through the updraft down to the melting level and encounter supercooled liquid water leading to riming in the layer just above the melting level. The riming only occurs on the larger masses of the crystals initialized at 6 km altitude, as the larger mass allows the crystals to more easily collect supercooled liquid water.

Until interacting with the strong updraft at 110° azimuth, FC3 has more columnar-like growth. Once it reaches the updraft, more plate-like growth occurs for the rest of its lifetime, especially for the last 2500 seconds. Additionally, the mass increases rapidly near the end of its lifetime as a result. The ICTG model is still modeling a spheroid, but at that point the aspect ratio is changing as the crystal grows in different dimensions. This may be representative of a capped crystal habit. The crystal initially grows as a column and

then grows more horizontally as the plate growth occurs (Pasquier et al., 2023; Libbrecht, 2005). This could be evidence that the ICTG model can model extremely complex ice crystal morphology.

At the end of its lifetime, between 9000 and 10,250 seconds, FC3 rapidly decreases in altitude (Figure 3.5d), decreases in ice supersaturation (Figure 3.5c), and increases in temperature (Figure 3.5b) before reaching the melting level. The crystal experiences sublimation and therefore a decrease in mass (Figure 3.5f). It is located in downdraft regions with negative vertical velocity (Figure 3.5h). The crystal reaches the melting level once reentering the upshear-right quadrant of the TC.

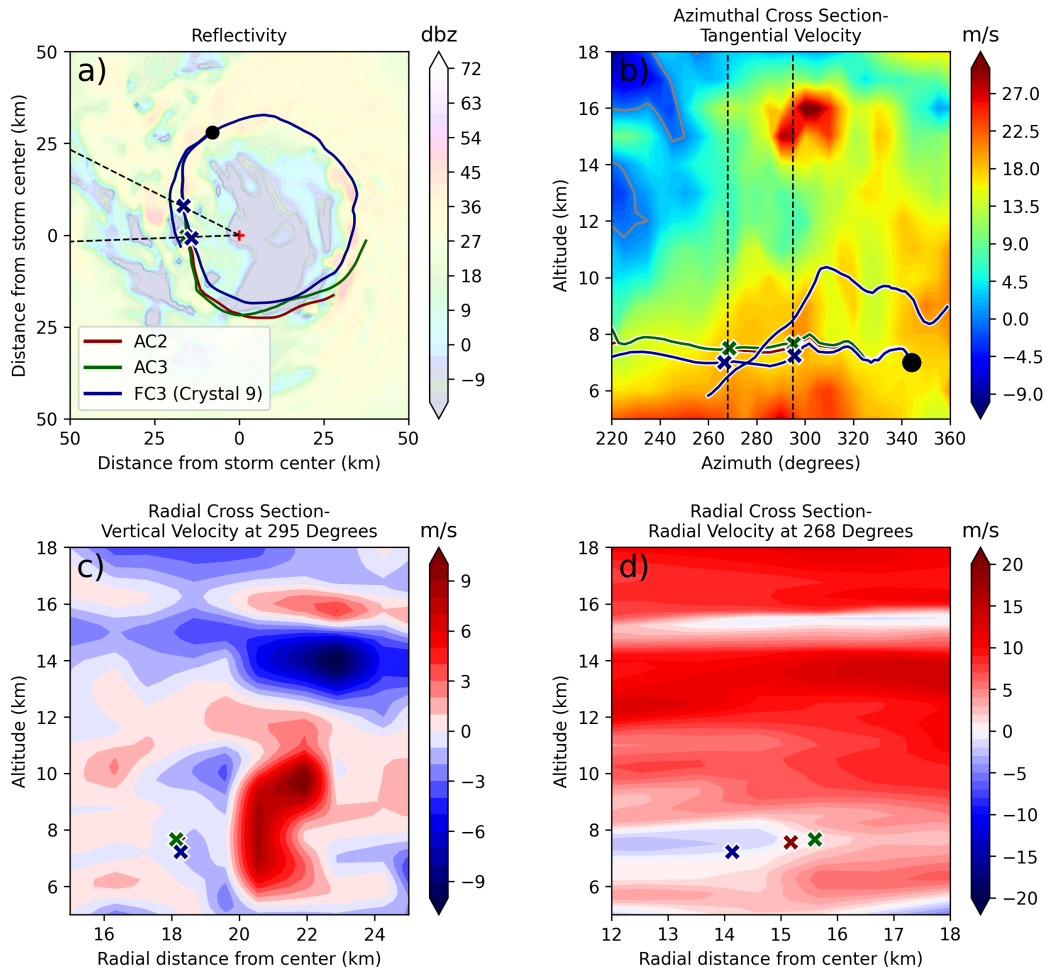


Figure 3.6. Crystals are initialized at the dot. Colored trajectories denote different initial size bins. Reflectivity in (a) at 6.5 km altitude. Azimuthal cross section (b) with tangential velocity radially averaged between 13 km and 18 km radius. Radial cross sections (c and d) along dashed lines in (a and b) at 295° azimuth (1040 seconds) and 268° azimuth (1440 seconds).

Only using time series, such as Figure 3.5, is limiting in that contextual details can be lost. Therefore, analyzing cross sections of the tropical cyclone provides crucial spatial context, allowing for a clearer interpretation of the environmental, dynamical, and thermodynamical factors that influence crystal behavior. This spatial perspective helps identify features that may be obscured in purely temporal analyses. It is important to analyze cross sections of the TC to better understand the specific potential causes of crystal behavior. One example of the need for cross section analysis is the divergence point that occurs between FC3 and the ACs near the beginning of their lifetimes. Figure 3.5a highlights this divergence point in the upshear-right quadrant of the TC around 1500 seconds into the simulation.

Figure 3.6c and d shows two cross sections taken at 295° azimuth (1040 seconds) and 268° azimuth (1440 seconds), respectively, to analyze crystal behavior going into this divergence point. As seen in Figure 3.5d and Figure 3.5f, at 295° azimuth (1040 seconds), the ACs are located around 7 km and increasing in mass, while FC3 is slightly decreasing in altitude to about 6.5 km. All three crystals are located in a downdraft, but FC3 is located in a region of stronger negative vertical velocity (Figure 3.6c) at this time. Note that the ACs are nearly overlapping in Figure 3.6c. The relatively strong tangential winds, shown in Figure 3.6b, continue to move the crystals cyclonically until they reach 268° azimuth. As seen in Figure 3.6d, FC3 is located in a region of negative radial velocity corresponding to inflow towards the eye. Both ACs are located in more neutral regions of radial velocity. After this time, the ACs are ejected further from the center as seen in Figure 3.5i. This specific example demonstrates that the updrafts and downdrafts within a TC and the overall radial flow cause extreme crystal diversity as the crystals pass through an updraft.

Figure 3.7 shows three cross sections in the downshear-right quadrant corresponding to 4700 seconds for FC3 and ACs. The cross sections are at 110° azimuth for the FC, 123° azimuth for AC2, and 126° azimuth for AC3. As noted previously, at 4700 seconds, FC3 interacts with a strong updraft. The vertical velocity radial cross section (Figure 3.7b) displays that FC3 is located within a strong and deep updraft that is leaning radially outward. FC3 experiences a vertical velocity of around 10 m/s. This is also shown in Figure 3.5h. This updraft is a pretty typical updraft within the eyewall for this simulation. Additionally, Figure 3.7b shows that the crystal is located in regions of relatively strong tangential velocity continuing to cyclonically move the crystal around the TC. AC3 (located at Size Bin 4) is also located in a region of positive vertical velocity at this time

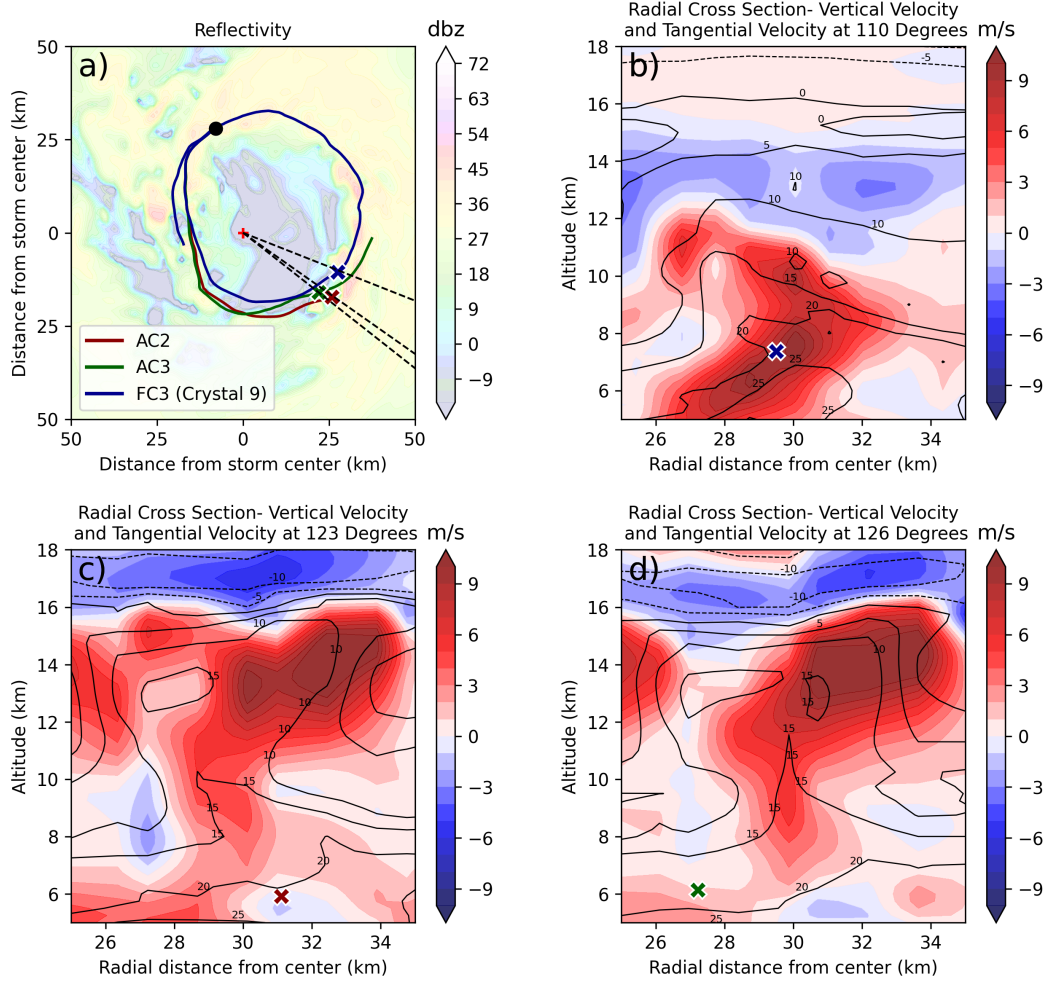


Figure 3.7. Crystals are initialized at the dot. Colored trajectories denote different initial size bins. Reflectivity in (a) at 6.5 km altitude. Radial cross sections (b, c, and d) along dashed lines in (a) at 110° azimuth, 123° azimuth, and 126° azimuth (4700 seconds). Tangential winds contoured at every 5 m/s.

shown in Figure 3.7d. It is also moving towards a stronger updraft that it experiences after this time elongating its lifetime. The vertical velocity it later experiences is similar in magnitude to the vertical velocity that FC3 experiences. As seen in Figure 3.5b, following the crystal interactions with the updrafts, FC3 is able to reach temperatures near -20° C, while AC3 only reaches temperatures around -8° C. AC3 is too heavy to stay lofted and quickly sinks to the melting level as shown in Figure 3.5b and Figure 3.5f. Meanwhile, FC3 continues to move cyclonically around the TC for a significant amount of time. AC2 (located at Size Bin 3) is located in a region of weak negative vertical velocity at this

time shown in Figure 3.7c. In addition to being in the region of negative vertical velocity pushing it lower in the atmosphere, it is also nearing the melting level and melts shortly after this timestep.

This group of crystals is a representative example of strong updrafts leading to size sorting of crystals and trajectory spread. These strong updrafts are a trigger that grows trajectory diversity and enhances diverging pathways. Small differences in crystals entering the updraft (or the crystals not entering the updraft at all) are enhanced and lead to the divergence of their trajectories and characteristics following their interaction with an updraft. This phenomena was observed near the beginning of these crystals' lifetimes in Figure 3.6 and once again, after over an hour, in Figure 3.7. At this second timestep, only a slight difference in crystal mass and location led to FC3 having its lifetime and azimuthal position be close to doubled compared to AC2 and AC3.

3.3 Multiple Unique and Extreme Crystals

Among the first two groups of crystals analyzed in this study, only minor differences in initial characteristics and the crystal's position at specific time steps led to substantial divergence in their subsequent evolution and behavior. These differences occurred even when crystals were initialized at the same location with only variations in initial mass. Interactions with dry eye air, the eyewall region, updrafts, and downdrafts aided in enhancing these differences. The final group of crystals examined in this analysis differs markedly from the other two groups. Although all crystals in this group were initialized at the same location, three of them developed notably distinct and extreme characteristics.

Figure 3.8 shows this group of crystals being initialized at 136° azimuth and 11 km altitude, but with different initial sizes. All three crystals follow very similar trajectories and have remarkably similar characteristics until they diverge in the downshear-left quadrant between 3000 and 5600 seconds. The crystal initialized at size bin 1 (referred to as FC4) with 3.62×10^{-5} mg initial mass reaches the second furthest radial distance of all crystals in this simulation at 130.37 km. Additionally, it is a long-lasting crystal — one of only five crystals that lasts until the end of the simulation (8 hours). The crystal initialized at size bin 2 (referred to as FC5) with 1.34×10^{-4} mg initial mass sublimates within the eye. Finally, the crystal initialized at size bin 3 (referred to as FC6) with 3.33×10^{-4} mg initial mass travels in vertical circular loops in both the radial and azimuthal directions for several hours during its lifetime. The three crystals are so closely grouped together

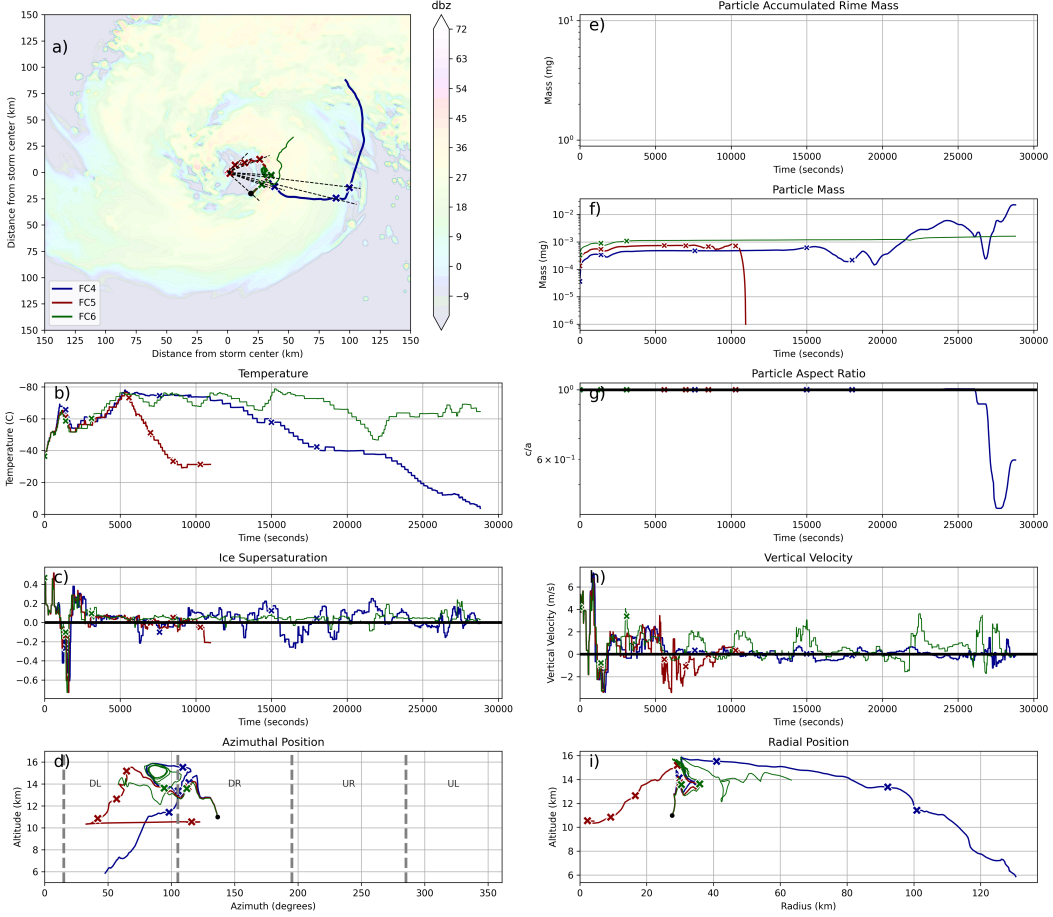


Figure 3.8. Crystals are initialized at the dot. Colored trajectories denote different initial size bins. Colored markers denote times when further analysis occurs. Reflectivity in (a) at 6.5 km altitude. Shear quadrants are marked in (d).

for the first 3000 seconds as they traverse the TC that they are located at nearly identical temperatures (Figure 3.8b), ice supersaturations (Figure 3.8c), azimuthal positions (Figure 3.8d), aspect ratios (Figure 3.8g), and radial positions (Figure 3.8i). The crystals all travel through a few updrafts up until 5000 seconds as seen in Figure 3.8h. Figure 3.8e shows that none of these crystals accumulate rime mass, which is expected given their initial altitudes. Their masses vary slightly (Figure 3.8f). It appears these slight differences in mass and vertical velocity are the causes for the differing behaviors in each crystal after approximately 3000 to 5600 seconds. Once again, only using time series is limiting in that specific details are lost. Therefore, we will analyze cross sections of the TC to provide crucial spatial context and a clearer interpretation of the environmental, dynamical, and thermodynamical factors that influence crystal behavior. Cross section analysis is needed

here to analyze the divergence that occurs between FC4, FC5, and FC6. Each of the crystals in Figure 3.8 will be further analyzed individually in this section.

Figure 3.9 shows azimuthal and radial cross sections of vertical velocity and radial velocity at select times and locations. At 0 seconds and 136° azimuth, the three crystals are firmly embedded within an updraft of around 3-6 m/s (Figure 3.9b, Figure 3.9c, and Figure 3.8h). They are also located within a region of weakly positive radial velocity of ~ 2 m/s causing them to be ejected slightly outward (Figure 3.9d and Figure 3.8i). As the crystals continue evolving, they reach 113° azimuth at 1400 seconds displayed in Figure 3.9e and Figure 3.9f. There is now a slight spread between the crystals with the smallest crystal, FC4, located at the highest altitude of the three. The largest crystal, FC6, is located at the lowest altitude of the three. They are spread out radially by < 1 km. This spread is expected given their sizes and findings from Chapter 3.2. It was noted that strong updrafts led to size sorting of crystals and trajectory spread. All three crystals are now located in a region of weak negative vertical velocity (0 to -3 m/s) as seen in Figure 3.9b and Figure 3.9e. The crystals are located at slightly larger radii than they were at the beginning of the simulation. Additionally, the crystals are experiencing inward radial velocity, which could be slowing down their outward trajectories shown in Figure 3.9f. After this timestep, between 3000 seconds and 5600 seconds, the three crystals diverge paths in the downshear-left quadrant.

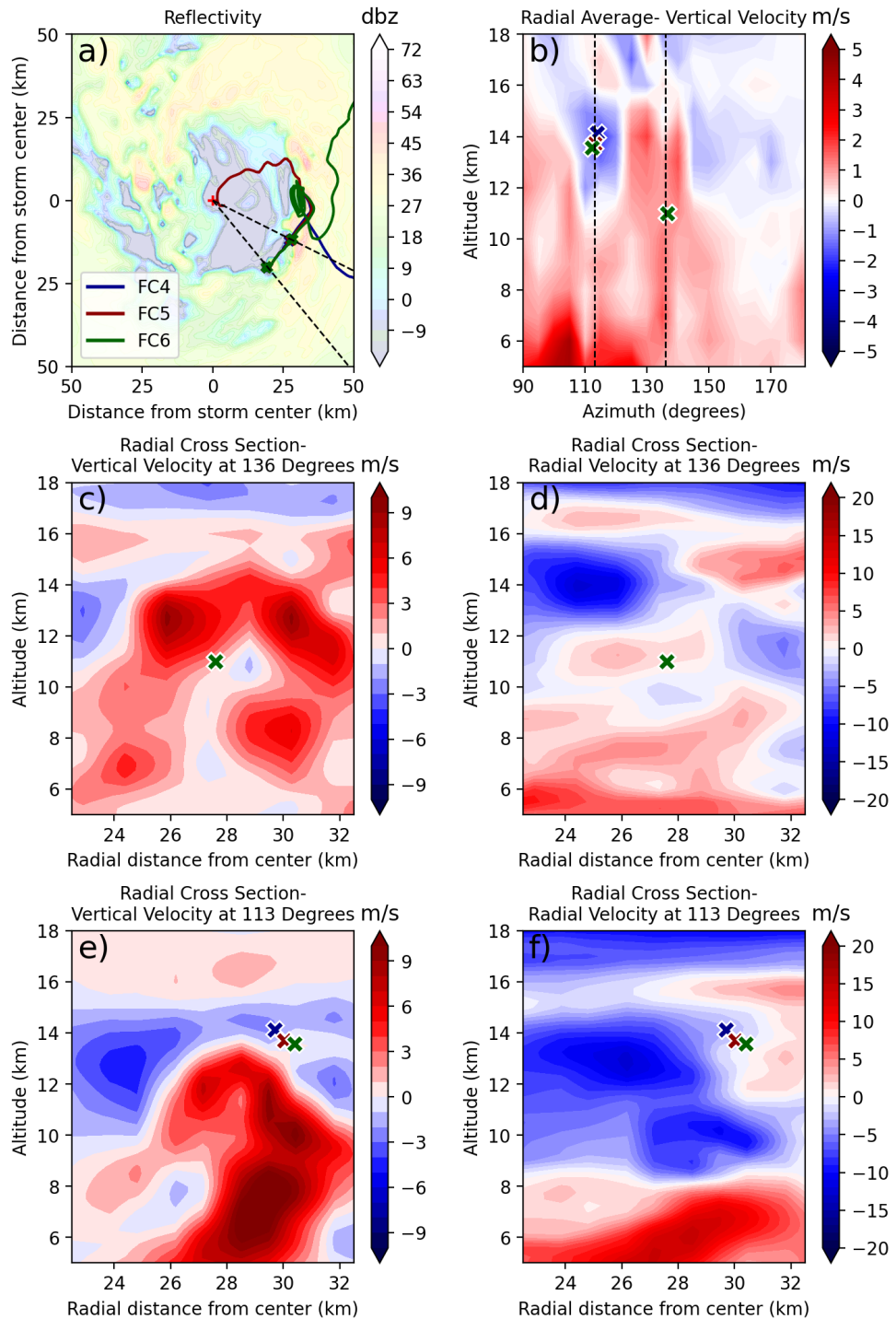


Figure 3.9. Crystals are initialized at the dot. Colored trajectories and markers denote different initial size bins. Reflectivity in (a) at 6.5 km altitude. Azimuthal cross section (b) with vertical velocity radially averaged between 22.5 km and 32.5 km radius. Radial cross sections (c, d, e, f) along dashed lines in (a) at 136° azimuth (0 seconds) in c and d and 113° azimuth (1400 seconds) in e and f.

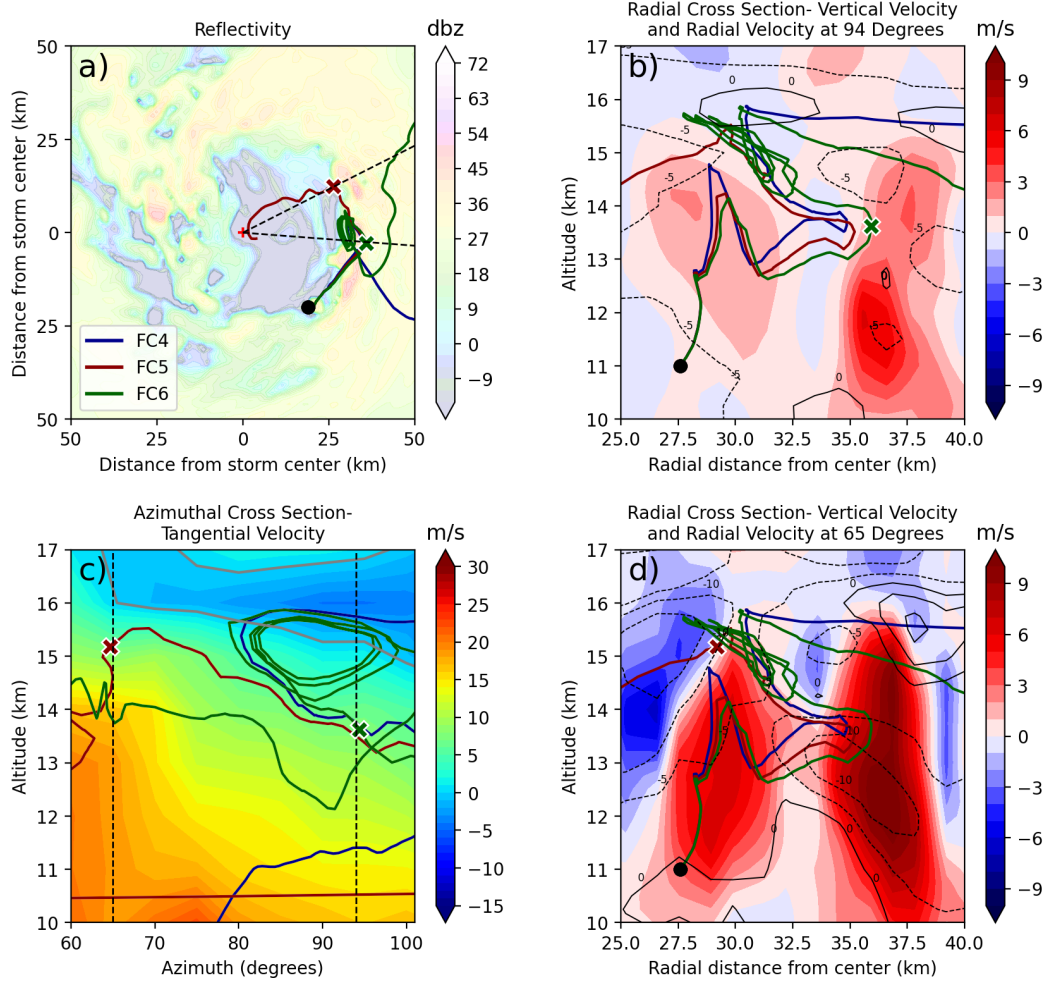


Figure 3.10. Crystals are initialized at the dot. Colored trajectories and markers denote different initial size bins. Reflectivity in (a) at 6.5 km altitude. Azimuthal cross section (c) with tangential velocity radially averaged between 25 km and 35 km radius. Radial cross sections (b and d) along dashed line in (a) at 94° azimuth (3100 seconds) in b and 65° azimuth (5580 seconds) in d. Radial velocity contoured at every 5 m/s in (b) and (d).

Next, we examine cross sections of the area where FC4, FC5, and FC6 diverge at 94° azimuth at 3100 seconds and at 65° azimuth at 5580 seconds to better understand the conditions that led to their divergent pathways. Figure 3.10 shows two radial cross sections of vertical velocity and radial velocity and an azimuthal cross section of tangential velocity. The three crystals enter this region in a size-sorted manner, with FC4 having the lowest mass and the highest altitude, while FC6 has the largest mass and is positioned at the lowest altitude. FC6 enters a region of approximately 4 m/s vertical velocity at this time (Figure 3.10b and Figure 3.8h). This allows FC6, which has a larger mass than FC4

and FC5, to reach a higher altitude than those two crystals after this time as seen in Figure 3.8b between approximately 3000 and 5000 seconds. After this point, FC5 continues at a slightly lower altitude than the other two crystals as all three crystals continue to rise in altitude. As a result, as shown in Figure 3.10d, FC5 reaches an area of negative vertical velocity of around -2 m/s.

Figure 3.10d displays a downdraft at the eye/eyewall interface. This figure also clearly shows the saturated downdraft present along the inner boundary of the eyewall updraft (with negative vertical velocity) located next to the updraft (with positive vertical velocity), at the interface between the eye and the eyewall. It is a common feature in TCs as described in Willoughby (1998); Black and Hallett (1986), and Didlake et al. (2017). At the eye/eyewall interface, the strong tangential and vertical winds of the eyewall meet the calmer winds of the eye. This forces turbulent mixing between the saturated, cloudy eyewall air with the unsaturated, dry eye air. The cloud droplets are then evaporated into the unsaturated air, which causes cooling, negative buoyancy, and sinking. Therefore, this results in a thin layer of negatively buoyant air that sinks and travels radially inward along the eye/eyewall interface (Willoughby, 1998). Meanwhile, during this same time period, FC4 and FC6 move into an area of negative tangential velocity as shown in Figure 3.10c. FC4 moves anticyclonically for over 10,000 seconds once it enters the area of negative tangential velocity.

Next, we examine cross sections focusing on each individual FC at multiple time steps to better understand the differing characteristics of the crystals following their divergence. Several cross sections were taken to analyze the behavior of FC4. As shown in Figure 3.8d and Figure 3.8i, the crystal gets lofted outwards and upwards after moving into the previously discussed region of negative tangential velocity and is experiencing weak positive vertical velocity of < 1 m/s between 4000 and 8000 seconds (Figure 3.8h). The first cross section focusing on FC4 is taken at 110° azimuth at 7600 seconds in Figure 3.11b. At this time, the crystal is located relatively high in the atmosphere near 16 km. FC4 is now located in the TC outflow layer, which is a narrow stripe of outflow near the tropopause, seen in the radial velocity field (Figure 3.11b). This is a normal TC feature that is necessary to conserve angular momentum of air parcels that are rising from the eyewall. Additionally, FC4 is being influenced by the upper level high located above the TC, which is also a normal feature of TCs. This feature is leading to the negative tangential winds that FC4 is embedded within as seen in Figure 3.11b. These winds lead to an anticyclonic turn in the trajectory of FC4 between around 4000 and 15,000 seconds,

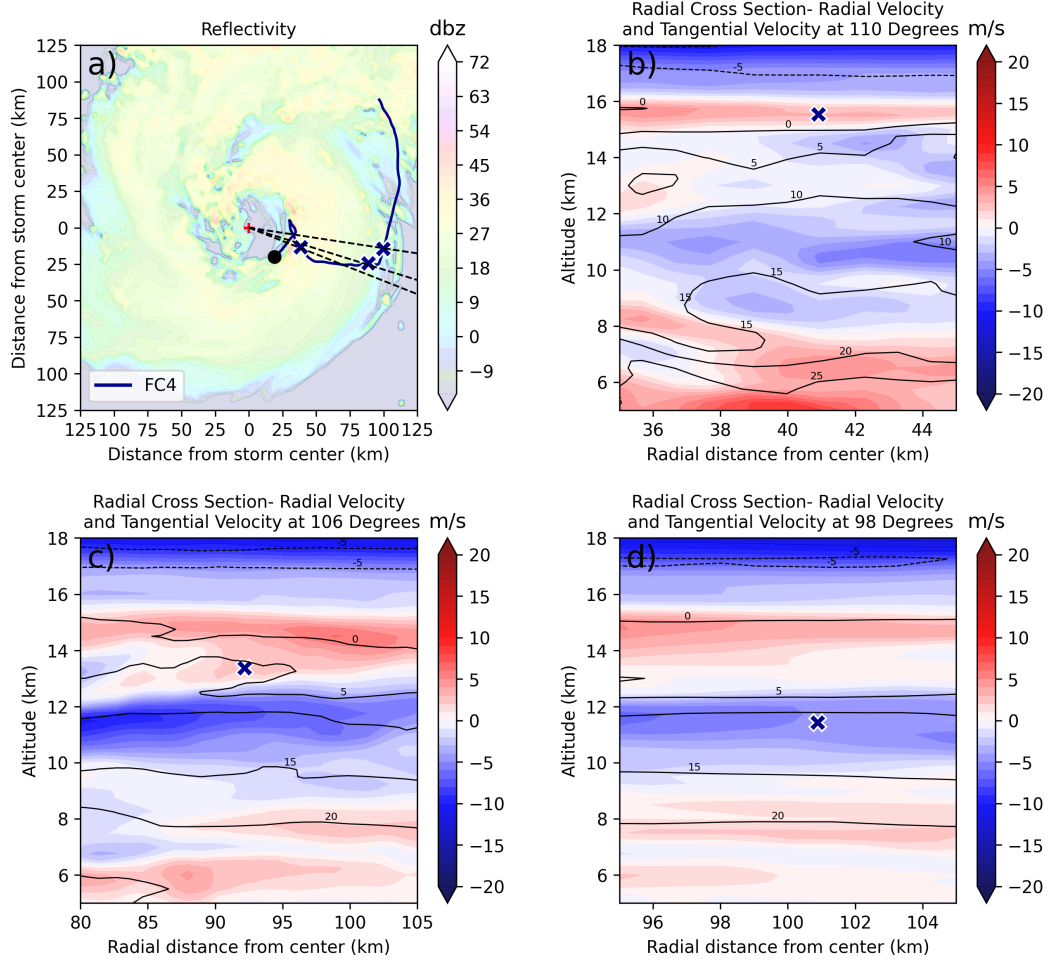


Figure 3.11. Crystal is initialized at the dot. Blue trajectories and markers denotes crystal initialized at size bin 1 (FC4). Reflectivity in (a) at 6.5 km altitude. Radial cross sections (b, c, and d) along dashed lines in (a) at 110° azimuth (7600 seconds) in b, 106° azimuth (15000 seconds) in c, and 98° azimuth (18000 seconds) in d. Tangential winds contoured at every 5 m/s in b, c and d.

clearly seen in its azimuthal position (Figure 3.8d). The radial outflow and slow fall speed of this crystal allows it to reach an extreme radial distance compared to the other crystals in this simulation.

FC4 continues to move in the anticyclonic flow for over 7,000 more seconds and has traveled nearly 50 km radially. This is demonstrated in Figure 3.8i- the radial position plot. It reaches the next cross section location at 106° azimuth at 15,000 seconds. Figure 3.11c shows that the crystal is no longer moving anticyclonically and has resumed moving cyclonically. Additionally, it has now sunk to the edge of the TC outflow layer and is down to about 13 km altitude. Finally, at 18,000 seconds, the crystal is located at 98°

azimuth. It is continuing to move cyclonically and is in a region of inflow (Figure 3.11d). The crystal continues to move cyclonically and reaches a final radial distance of 130.37 km (Figure 3.8i). It reaches the end of the simulation after 8 hours.

Overall, normal TC features, such as the TC outflow layer and the upper-level high located above the TC, influence the movement of this crystal, with the radial outflow, in particular, allowing it to reach such an extreme final radial distance. This analysis highlights how TC features can affect individual crystal trajectories within the storm, which is important for linking those trajectories and characteristics to storm-scale dynamics.

Now, we will analyze several cross sections of FC5 after it has diverged from FC4 and FC6. Once FC5 enters the aforementioned area of negative vertical velocity between 5000 and 7000 seconds, it quickly increases in temperature (Figure 3.8b) and decreases in altitude (Figure 3.8d). In the first cross section, at 7000 seconds, FC5 is located at 56° azimuth. It is located within the eye as seen in Figure 3.12a. As a result, FC5 is interacting with subsaturated air that has an ice supersaturation of around -0.05 at this time (Figure 3.12b and Figure 3.8c). The eye is dry, which causes the crystal to sublimate. This is seen in Figure 3.8f with some small decreases in FC5's mass noted around this time period. Additionally, the crystal is located in a weak downdraft region (around -1 m/s) and a region of negative radial velocity (around -5 to -10 m/s) shown in Figure 3.12c. This causes the crystal to slowly sink in altitude and move closer to the center of the eye as seen in Figure 3.8i.

At 8500 seconds, FC5 is now located at 42° azimuth. The same environmental influences are at play: the crystal is located in a region of negative ice supersaturation, a region of weak downdrafts, and a region of weak inflow (Figure 3.12d and Figure 3.12e). FC5 is now located in a region of about -0.1 ice supersaturation, which is lower than it was at the last timestep. Finally, at 10,300 seconds, the crystal is located at 105° azimuth. The crystal is located in an environment that is extremely subsaturated (Figure 3.12f) with vertical velocity near zero and weak inflow (Figure 3.12g). The ice supersaturation is even lower at this time- around -0.2. The further reduction in ice supersaturation relative to the previous timesteps is attributed to the crystal's proximity to the TC center. As the crystal approaches the center of the eye, it encounters increasingly drier air, leading to more negative ice supersaturation values. The negative ice supersaturation, also shown in Figure 3.8c, causes the steep decline in mass seen in Figure 3.8f. Overall, the ice supersaturation is negative for large portions of the SB2's lifetime and the crystal never reaches the melting level. Instead, it sublimates within the eye around 10 km altitude quite

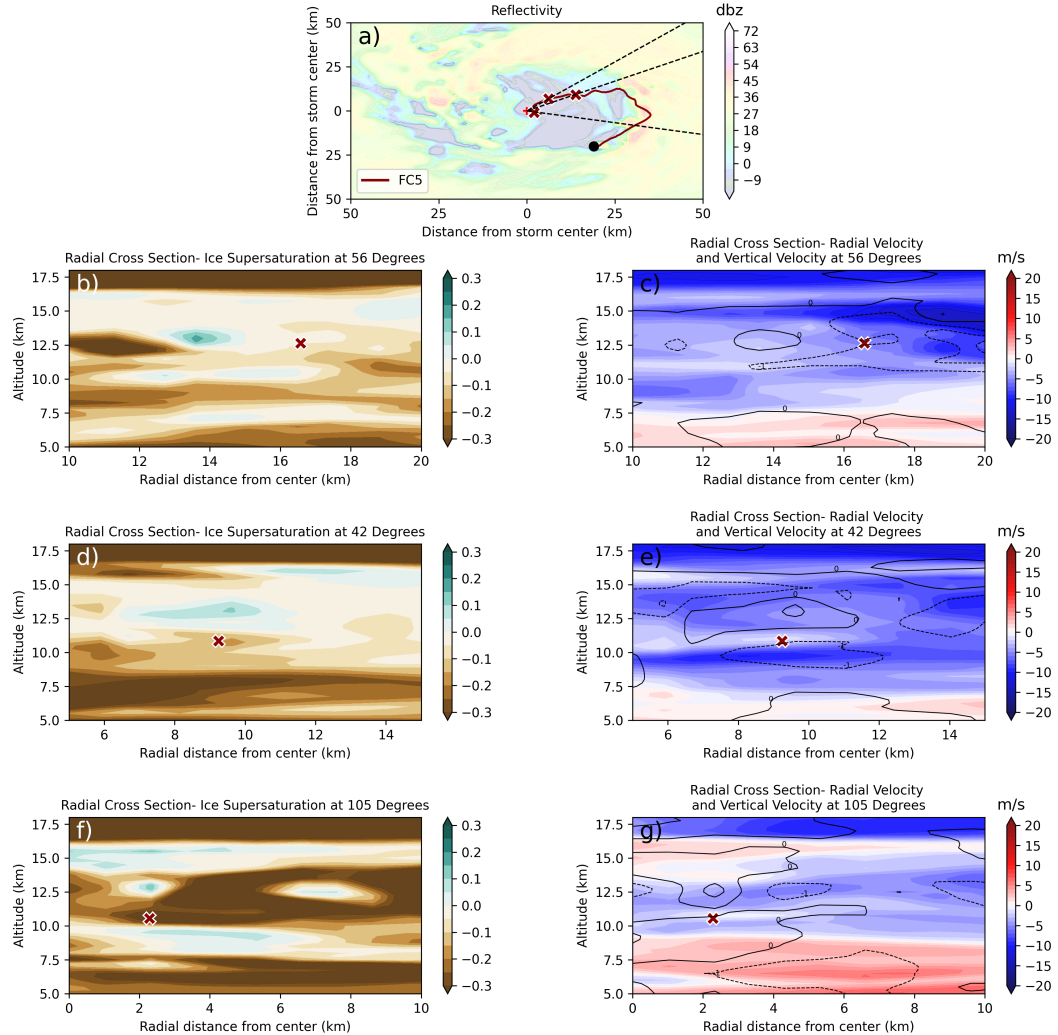


Figure 3.12. Crystal is initialized at the dot. Red trajectories and markers denotes crystal initialized at size bin 2 (FC5). Reflectivity in (a) at 6.5 km altitude. Radial cross sections (b-g) along dashed lines in (a) at 56° azimuth (7000 seconds) in b and c, 42° azimuth (8500 seconds) in d and e, and 105° azimuth (10300 seconds) in f and g. Vertical velocity contoured at every 1 m/s in c, e, and g.

rapidly after 10,000 seconds, due to being located in the region of extremely negative ice supersaturation.

Finally, FC6 is further analyzed using cross sections. Once FC6 enters the aforementioned area of negative tangential velocity around 4000 seconds, it acquires unique radial and azimuthal looping features. Thermodynamic conditions and crystal characteristics play a critical role in sustaining the looping behavior of FC6. Cross sections taken straight through the center of the looping of the crystal help to analyze potential reasons

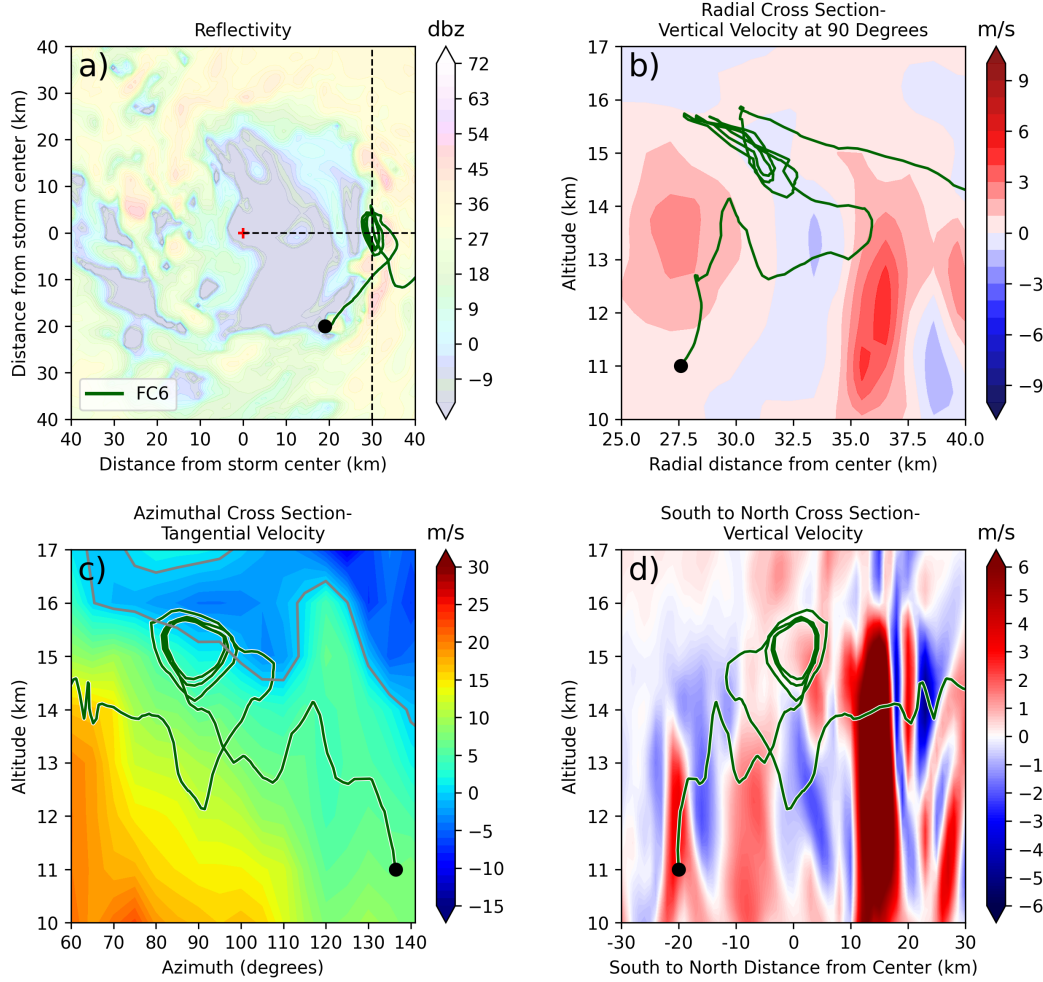


Figure 3.13. Crystal is initialized at the dot. Green trajectories and markers denotes crystal initialized at size bin 3 (FC6). Reflectivity in (a) at 6.5 km altitude. Vertical Velocity radial cross section (b) is along dashed line in (a) originating at the center of TC. Azimuthal cross section (c) with tangential velocity radially averaged between 25 km and 40 km radius. Vertical Velocity south to north cross section (d) is along dashed line in (a) running from south to north.

for this unique behavior. In Figure 3.13a, the crystal moves counterclockwise through the loop along the inner edge of the eyewall reflectivity. The radial looping behavior and oscillatory motion of FC6 are a result of the crystal interacting with the eye/eyewall interface and the upper-level anticyclonic winds. Initially, FC6 moves inwards towards smaller radial distances before reversing directions and moving outward towards larger radial distances (Figure 3.8i). Additionally, the crystal remains suspended near the top of an updraft seen in Figure 3.13b. In Figure 3.13c, the crystal moves clockwise through the loop. The radially averaged tangential velocity in Figure 3.13c clearly delineates

the boundary between regions where the crystal is being advected towards increasing azimuthal angles (anticyclonic winds indicated by negative tangential velocity values) and regions where it is moving towards decreasing azimuthal angles (cyclonic winds indicated by positive tangential velocity values). The crystal loops over 3 times, oscillating along different radii and azimuths, between 14 and 16 km altitude. It takes around an hour for the crystal to complete one full loop with one loop covering approximately 7 to 10 km. The crystal's mass remains relatively stable in Figure 3.8f throughout this looping pattern, suggesting minimal growth, which is one of the key reasons it stays in the loop. Due to its high altitude and the presence of unfavorable environmental conditions for substantial growth, the crystal maintains a nearly constant size, allowing it to remain trapped within the loop. If the crystal had gained substantial mass, it would have likely fallen in altitude and exited the looping pattern. There are several increases in vertical velocity (Figure 3.8h), keeping the crystal lofted until the end of the simulation. There are subsequent fluctuations in altitude (Figure 3.8d) and ice supersaturation (Figure 3.8c). The vertical velocity component in Figure 3.13d shows that the crystal is rising in the stronger part of updraft and sinking in the weaker part of updraft.

Overall, the interaction between thermodynamic conditions (e.g., temperature and supersaturation), crystal mass, and dynamic wind fields supports the crystal's sustained looping trajectory. This particular crystal highlights how localized environmental conditions and internal eyewall structure can cause crystals to recirculate. The combination of changing thermodynamic conditions and dynamic wind patterns demonstrates the complex interactions between TC dynamics and microphysics within the eyewall region of TCs.

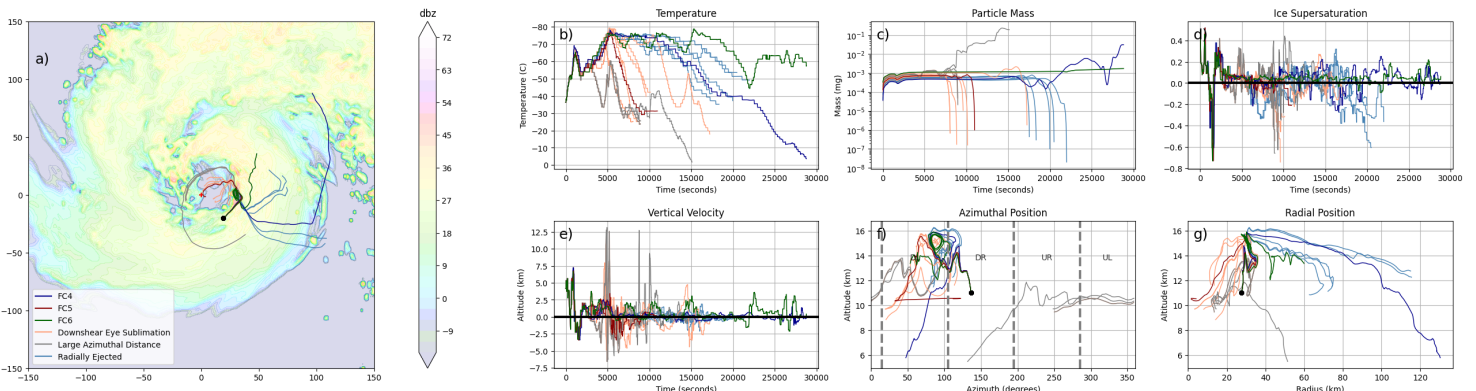


Figure 3.14. Crystals are initialized at the dot. Colored trajectories denote different initial size bins. Reflectivity in (a) at 6.5 km altitude. Shear quadrants are marked in (f).

To further evaluate the sensitivity of the initial crystal mass, we ran new simulations of crystals initialized at the same initialization location as FC4, FC5, and FC6. While FC4, FC5, and FC6 represented the 10th, 30th, and 50th percentiles of the IWC, we ran new crystals between the 10th and 50th percentiles, evenly dividing this span by 18 (yielding a percentile interval of 2.22), coming to a total of sixteen new crystals. Figure 3.14 shows these new trajectory results. We sort the crystals other than FC4, FC5, and FC6 into three categories based on their trajectories: Downshear Eye Sublimation, Large Azimuthal Distance, and Radially Ejected. Downshear Eye Sublimation crystals sublimate within the eye near the center of the TC. Large Azimuthal Distance crystals complete at least $\frac{3}{4}$ revolution around the TC and either sublimate or melt. Finally, Radially Ejected crystals complete one small loop, are radially ejected, and then sublimate further out in the TC. These behaviors differ based on ice crystal size and location throughout the simulation. During approximately the first 2500 seconds of the simulation, all 16 crystals exhibit broadly similar behavior and characteristics. The crystals have ice supersaturations that fluctuate between positive and negative values (Figure 3.14d) and are immediately lofted above 15 km altitude or around -60°C (Figure 3.14b and Figure 3.14g). They have similar vertical velocities (Figure 3.14e), as well. Azimuthally, the crystals move from approximately 140° to 90° , moving from the downshear-right quadrant to the downshear-left quadrant (Figure 3.14f). Radially, the crystals remain between 25 and 35 km radius for much of this time (Figure 3.14g). After this initial time period, the crystals begin to diverge as shown in Figure 3.14f and Figure 3.14g. There are three different divergence points between the crystals creating the named groups that will be further analyzed.

In Figure 3.16a, we compare the trajectories and behaviors of Crystal 14 and Crystal 15. Crystal 14 is a downshear eye sublimation crystal, is initialized at the 27.78 percentile of the IWC distribution, and sublimates near the eye center. Crystal 15 is a large azimuthal distance crystal, is initialized at the 38.89 percentile of the IWC distribution, and completes nearly three-quarters of a revolution before sublimating further out. As shown in Figure 3.15c, Crystal 15 is heavier than Crystal 14 initially and at the location of the cross section (seen in Figure 3.15a). Crystal 15 initializes with a mass of 2.56×10^{-4} mg, while Crystal 14 initializes with a mass of 1.34×10^{-4} mg. Thus, Crystal 15 is influenced more by the negative vertical velocity (downdrafts) as seen in Figure 3.15d and Figure 3.16a. As a result, beginning at approximately 3500 seconds, Crystal 15 sinks in altitude to around 11 km while Crystal 14 continues increasing in altitude until

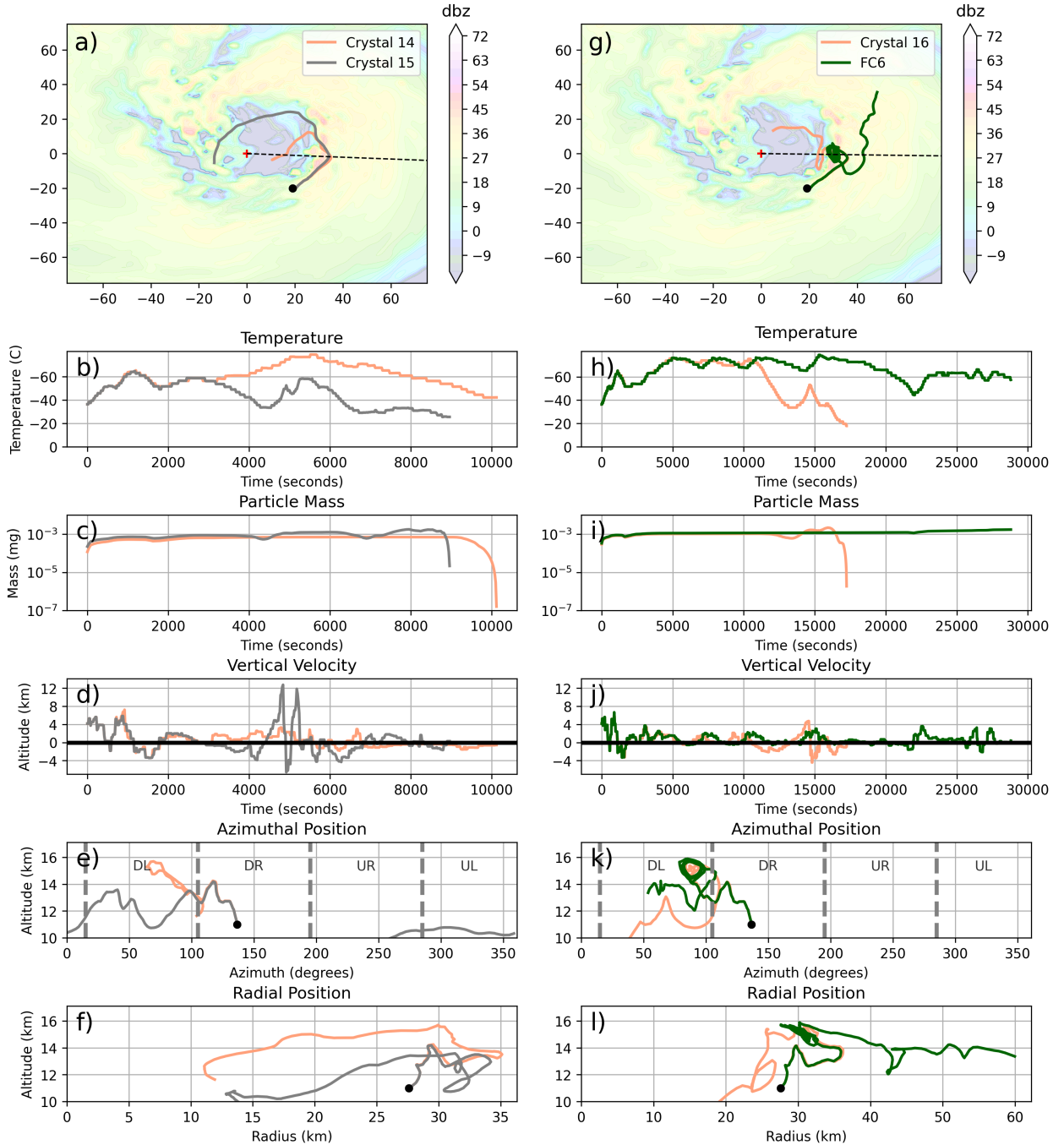


Figure 3.15. Crystals are initialized at the dots. Colored trajectories denote crystals- Crystal 14 and Crystal 15 in (a-f) and Crystal 16 and FC6 in (g-l). Reflectivity in (a) and (g) at 6.5 km altitude. Radial cross sections in Figure 3.16 are along dashed lines in (a) and (g) at 93° azimuth and 91° azimuth. Shear quadrants are marked in (e) and (k).

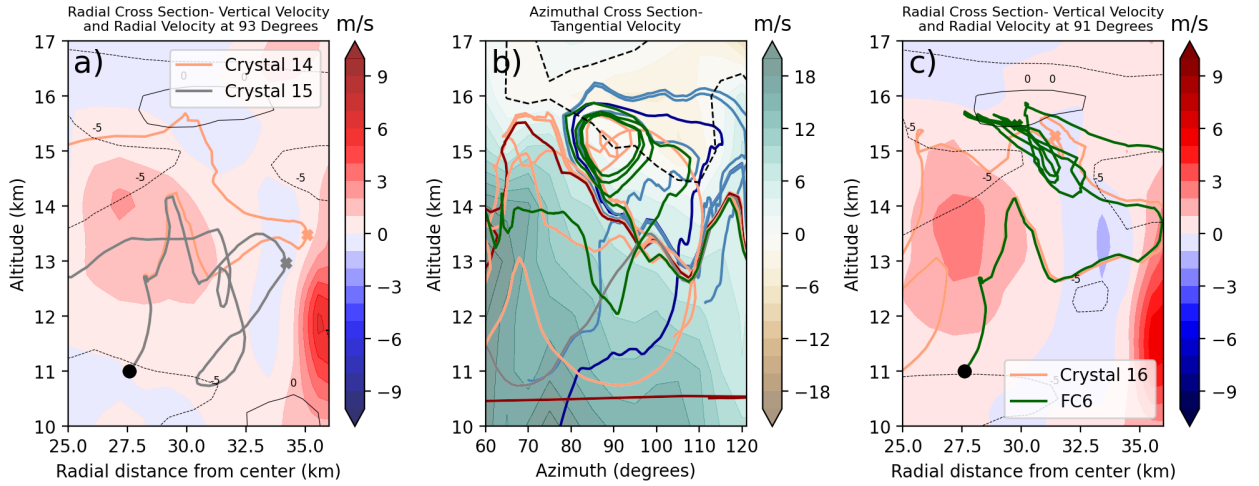


Figure 3.16. Crystals are initialized at the dots. Colored trajectories and markers denote different initial size bins. Azimuthal cross section (b) with tangential velocity radially averaged between 25 km and 35 km radius. Dashed line in (b) denotes 0 m/s tangential velocity. Radial cross sections (a and c) at 93° azimuth in (a) and 91° azimuth in (c). Radial velocity contoured at every 5 m/s in (a) and (c).

entering the region of negative tangential velocity as illustrated in Figure 3.15e and Figure 3.16b. In Figure 3.16b, crystals that sublime in the eye are a little lower in azimuth and altitude than those that end up sublimating further out in the TC. This is due to size sorting occurring. The lighter crystals are lofted higher than the heavier crystals. The crystals that sublime in the eye do not enter the area of negative tangential velocity and are thus continuing to move cyclonically. These crystals enter an aforementioned area of negative vertical velocity between 5000 and 7000 seconds on the eye/eyewall interface. The ice crystals quickly increase in temperature (Figure 3.14b) and decrease in altitude (Figure 3.14f) similar to the behavior of FC5.

Figure 3.16c shows a comparison between a downshear eye sublimation crystal (Crystal 16) and FC6. Crystal 16 is initialized at the 45.56 percentile of the IWC distribution and has an initial mass of 2.92×10^{-4} mg. FC6 has an initial mass of 3.33×10^{-4} mg. Thus, Crystal 16 has a smaller initial mass and stays smaller than FC6 for much of its lifetime (Figure 3.15i). As seen most clearly in Figure 3.15k, Crystal 16 completes 2 smaller loops in the downshear-left quadrant before getting ejected into the eye and sublimating. Meanwhile, FC6 completes three large loops before getting ejected out radially and sublimating. The radial position plot (Figure 3.15l) clearly shows these differences in the crystal's radial positions throughout their lifetime. The two crystals

begin to diverge around 5,800 seconds when Crystal 16 moves back into the region of positive tangential velocity before FC6 does as seen in Figure 3.16b. Additionally, both crystals loop near the boundary between positive and negative tangential velocity in that figure. As seen in Figure 3.16c, FC6 continues floating on the top of an updraft — it is located more on top of the updraft than Crystal 16 — until getting ejected radially.

Overall, this sensitivity test shows that the five ice crystals at the 10th, 30th, 50th, 70th, and 90th percentiles of the IWC distribution are a representative sample. By initializing additional crystals, we confirm that there are clear differences in the behavior and characteristics of the ice crystals as their initial size is altered. These results underscore the importance of explicitly resolving initial size variability of ice crystals in ice microphysical modeling for TCs.

Furthermore, the crystals analyzed in this study represent a subset of some extreme and unique ice crystals simulated by the ICTG model. Within the TC eyewall, even minor spatial variations in the environment and/or slight differences in initial crystal size could lead to diverse trajectories and differing crystal characteristics. Strong updrafts play a key role in this process, promoting size sorting, and spreading crystal paths. These updrafts act as a trigger, amplifying small initial differences, and producing divergent outcomes based on whether a crystal enters the updraft, the timing of entering the updraft, and/or its mass.

Crystals that attained exceptionally large mass and low aspect ratios in Chapter 3.1 did so through extreme dendritic growth. These crystals remained within the dendritic growth zone (DGZ) and were exposed to strong vertical velocities for large portions of their lifetimes, encouraging rapid plate-like growth. Crystals in Chapter 3.2 completed one or more revolutions around the TC due to their interactions with weak to moderate updrafts and their relatively low ice supersaturation and mass, which allowed them to remain lofted. Finally, in Chapter 3.3, the crystal that reached large final radial distances was influenced by anticyclonic flow. In contrast, the crystal that sublimated within the eye was exposed to extremely dry conditions and persistently negative ice supersaturation. The final crystal analyzed exhibited looping behavior in both radial and azimuthal directions, primarily due to its interactions with the eye/eyewall interface and anticyclonic flow.

Altogether, this analysis underscores the complexity of individual crystal behavior within the TC environment, specifically for those crystals initialized within the eyewall. Some key storm-scale features, including strong updrafts and downdrafts, the upper-level high above the TC, upper-level outflow, downdrafts on the inner edge of the eyewall, and

dry subsiding air in the eye, play a central role in shaping the evolution and trajectories of ice crystals within the TC. Recognizing and understanding these influences is essential for linking microphysical properties and ice crystal trajectories to larger-scale TC dynamics and for improving our understanding of TC structure, intensity, and strength.

Chapter 4

Conclusions

In this thesis, we applied the Ice Crystal Trajectory (ICTG) model to the eyewall region of a simulated Hurricane Harvey (2017) to analyze how both the ice crystal environment and the ice crystal properties evolve over time. Specifically, we examined unique and extreme ice crystals simulated within Hurricane Harvey to better understand the full range of possibilities for an ice crystal initialized in a TC eyewall. It was hypothesized that the ICTG model would show that small spatial variations within the environment and the initial crystal size would create varied trajectory paths and differing crystal properties.

The ICTG model developed by Laurencin et al. (2022) is unique in that it provides individual ice crystal tracking using the Lagrangian approach. The model uses data input from the PSU WRF-EnKF model, such as winds, temperature, humidity, and reflectivity. The ICTG model initializes five crystals of varying sizes based on the particle size distributions at each specified location and tracks the properties of individual ice crystals at each time step. Further analysis was conducted to investigate the behavior of several crystals and the environmental factors influencing their evolution.

We conclude that the ICTG model is able to model realistic and reasonable paths for ice crystals located within the TC eyewall, even though the model has some limitations, such as a lack of aggregation and secondary ice production. This study examined ice crystals with extreme characteristics, such as the largest mass, longest-lasting, lowest aspect ratio, and furthest final radial distance, as well as unique characteristics, including sublimation within the eye, completing one or more revolutions, and cycling both radially and azimuthally. The crystals analyzed in this study represent a subset of some extreme and unique ice crystals simulated by the ICTG model, though they exhibited several common characteristics that are representative of all simulated ice crystals. For instance, crystals that are located within regions of positive ice supersaturation and/or within the

dendritic growth zone (DGZ) grow quite efficiently as demonstrated in Chapter 3.1. The DGZ, specifically, allows efficient crystal growth via vapor deposition and is favorable for plate-like growth and low aspect ratios. In Chapter 3.2, it was found that long-lived crystals sustain themselves by remaining relatively small in mass for extended periods and passing through multiple updrafts (regions of positive vertical velocity), which enables continued growth. Finally, in Chapter 3.3, it was shown that the eye is a region dominated by areas of negative ice supersaturation, weak downdrafts, and weak inflow, which encourages the ice crystals to sublimate once they move into the eye.

This analysis showed that within the eyewall alone, small spatial variations within the environment and small variations in the initial crystal size created varied trajectory paths and differing crystal properties. Strong updrafts are one main cause of this crystal diversity. In particular, crystals of different initial sizes that encounter the same updraft attain a large spread in the trajectories and characteristics of those ice crystals, and in some cases, size sorting. There were numerous cases in this analysis of these updrafts acting as a trigger, amplifying small initial differences, and producing divergent outcomes based on whether a crystal enters the updraft, the timing of entering the updraft, and/or its mass, such as in Chapter 3.2. In Chapter 3.3, the crystal that reached a large final radial distance was influenced by anticyclonic flow. Another crystal in Chapter 3.3 exhibited looping behavior in both the radial and azimuthal directions, primarily due to its interactions with the eye/eyewall interface and anticyclonic flow above the TC, which is common in all TCs.

Overall, this study highlights the intricate and variable nature of ice crystal behavior within a TC, particularly for crystals originating in the eyewall region. Several prominent storm-scale features, including strong updrafts and downdrafts, the upper-level high above the TC creating anticyclonic flow, upper-level outflow, downdrafts on the inner edge of the eyewall, and dry, and subsiding air in the eye were found to strongly influence the evolution and characteristics of individual ice crystals. Analyzing the interactions between these features and the ice crystals is crucial for connecting microphysical processes and crystal trajectories to broader TC dynamics and in advancing our understanding and prediction of tropical cyclone structure and intensity.

The spatial information seen here in ice crystal trajectory modeling is important because the location of where crystals grow can affect where in the hurricane that latent heat release and latent cooling occurs which, in turn, can affect the overall strength of the TC. For instance, locations where ice melts, including where ice crystals reach the

melting level in the ICTG model, are favorable locations for stratiform precipitation to occur. Modeling the correct crystal shape also affects the radiative properties of the cirrus shield. Radiative properties can affect the overall stability of the clouds structures, impacting whether new convection initiation is preferred or if stratiform cloud decks and their precipitation are prolonged. When crystals reach distances further out from the center, this affects how large the cirrus shield of a tropical cyclone can become. Additionally, the location of ice in the TC will affect the longwave radiation emitted by the clouds. As shown in this analysis, if we can better model ice crystal trajectories, we can better parameterize the ice microphysics, especially within TCs. This will allow us to better understand the cold phase region of a TC and better predict overall TC intensity through improving trajectory modeling.

Future work could include the use of different microphysics schemes in the ICTG model. Additionally, the ICTG model could be applied to different scenarios. This could include investigating the rainbands within Hurricane Harvey and/or investigating other hurricanes. These results would then be used to compare and contrast ice crystal properties and behavior with the current Hurricane Harvey eyewall-focused analysis.

In conclusion, these new findings demonstrate ice microphysical processes that are not fully captured in weather models. This research adds to our current understanding of modeling ice microphysics within TCs as forecasting TCs is highly dependent on how ice microphysics are modeled. The ICTG model is useful in providing a more explicit representation of ice crystals and their growth properties and processes due to the use of a Lagrangian framework. In the future, this research could lead to potential improvements to the ice microphysics in weather forecast models, including predictions of intensity and structural changes of tropical cyclones.

Bibliography

- Bender, M. A., 1997: The effect of relative flow on the asymmetric structure in the interior of hurricanes. *Journal of the Atmospheric Sciences*, **54**, 703–724, doi:10.1175/1520-0469(1997)054<0703:TEORFO>2.0.CO;2.
- Black, R. A., 1990: Radar reflectivity-ice water content relationships for use above the melting level in hurricanes. *Journal of Applied Meteorology and Climatology*, **29**, 955 – 961, doi:10.1175/1520-0450(1990)029<0955:RRIWCR>2.0.CO;2.
- Black, R. A. and J. Hallett, 1986: Observations of the distribution of ice in hurricanes. *Journal of Atmospheric Sciences*, **43**, 802 – 822, doi:10.1175/1520-0469(1986)043<0802:OOTDOI>2.0.CO;2.
- 1999: Electrification of the hurricane. *Journal of the Atmospheric Sciences*, **56**, 2004 – 2028, doi:10.1175/1520-0469(1999)056<2004:EOTH>2.0.CO;2.
- Blake, E. S. and D. A. Zelensky, 2018: Tropical cyclone report hurricane harvey (2017), 1–77.
- Brdar, S. and A. Seifert, 2018: McSnow: A Monte-Carlo Particle Model for Rimming and Aggregation of Ice Particles in a Multidimensional Microphysical Phase Space. *J. Adv. Model. Earth Syst.*, **10**, 187–206, doi:10.1002/2017MS001167.
- Bryan, G. H. and H. Morrison, 2012: Sensitivity of a simulated squall line to horizontal resolution and parameterization of microphysics. *Monthly Weather Review*, **140**, 202 – 225, doi:10.1175/MWR-D-11-00046.1.
- Cecil, D. J. and E. J. Zipser, 2002: Reflectivity, ice scattering, and lightning characteristics of hurricane eyewalls and rainbands. part ii: Intercomparison of observations. *Monthly Weather Review*, **130**, 785 – 801, doi:10.1175/1520-0493(2002)130<0785:RISALC>2.0.CO;2.
- Cholette, M., H. Morrison, J. A. Milbrandt, and J. M. Thériault, 2019: Parameterization of the bulk liquid fraction on mixed-phase particles in the predicted particle properties (p3) scheme: Description and idealized simulations. *Journal of the Atmospheric Sciences*, **76**, 561 – 582, doi:10.1175/JAS-D-18-0278.1.

- Corbosiero, K. L. and J. Molinari, 2002: The effects of vertical wind shear on the distribution of convection in tropical cyclones. *Monthly Weather Review*, **130**, 2110–2123, doi:10.1175/1520-0493(2002)130<2110:TEOVWS>2.0.CO;2.
- 2003: The relationship between storm motion, vertical wind shear, and convective asymmetries in tropical cyclones. *Journal of the Atmospheric Sciences*, **60**, 366–376, doi:10.1175/1520-0469(2003)060<0366:TRBSMV>2.0.CO;2.
- DeHart, J. C., R. A. Houze, and R. F. Rogers, 2014: Quadrant distribution of tropical cyclone inner-core kinematics in relation to environmental shear. *Journal of the Atmospheric Sciences*, **71**, 2713 – 2732, doi:10.1175/JAS-D-13-0298.1.
- Didlake, A. C., G. M. Heymsfield, P. D. Reasor, and S. R. Guimond, 2017: Concentric eyewall asymmetries in Hurricane Gonzalo (2014) observed by airborne radar. *Monthly Weather Review*, **145**, 729–749, doi:10.1175/MWR-D-16-0175.1.
- Didlake, A. C. and M. R. Kumjian, 2017: Examining polarimetric radar observations of bulk microphysical structures and their relation to vortex kinematics in hurricane arthur (2014). *Monthly Weather Review*, **145**, 4521 – 4541, doi:10.1175/MWR-D-17-0035.1.
- Didlake, A. C., P. D. Reasor, R. F. Rogers, and W. C. Lee, 2018: Dynamics of the transition from Spiral Rainbands to a secondary eyewall in Hurricane Earl (2010). *Journal of the Atmospheric Sciences*, **75**, 2909–2929, doi:10.1175/JAS-D-17-0348.1.
- Frank, W. M. and E. A. Ritchie, 1999: Effects of environmental flow upon tropical cyclone structure. *Monthly Weather Review*, **127**, 2044–2061, doi:10.1175/1520-0493(1999)127<2044:EOFUT>2.0.CO;2.
- Grabowski, W. W., H. Morrison, S. I. Shima, G. C. Abade, P. Dziekan, and H. Pawlowska, 2019: Modeling of cloud microphysics: Can we do better? *Bull. Am. Meteorol. Soc.*, **100**, 655–672, doi:10.1175/BAMS-D-18-0005.1.
- Harrington, J. Y., A. Moyle, L. E. Hanson, and H. Morrison, 2019: On calculating deposition coefficients and aspect-ratio evolution in approximate models of ice crystal vapor growth. *J. Atmos. Sci.*, **76**, 1609–1625, doi:10.1175/JAS-D-18-0319.1.
- Harrington, J. Y., K. Sulia, and H. Morrison, 2013: A method for adaptive habit prediction in bulk microphysical models. Part I: Theoretical development. *J. Atmos. Sci.*, **70**, 349–364, doi:10.1175/JAS-D-12-040.1.
- Hashino, T. and G. J. Tripoli, 2007: The spectral ice habit prediction system (ships). part i: Model description and simulation of the vapor deposition process. *Journal of the Atmospheric Sciences*, **64**, 2210 – 2237, doi:10.1175/JAS3963.1.

- Heymsfield, A. J., A. Bansemer, S. L. Durden, R. L. Herman, and T. P. Bui, 2006: Ice microphysics observations in hurricane humberto: Comparison with non-hurricane-generated ice cloud layers. *Journal of the Atmospheric Sciences*, **63**, 288 – 308, doi:10.1175/JAS3603.1.
- Hou, A. Y., R. K. Kakar, S. Neeck, A. A. Azarbarzin, C. D. Kummerow, M. Kojima, R. Oki, K. Nakamura, and T. Iguchi, 2014: The global precipitation measurement mission. *Bulletin of the American Meteorological Society*, **95**, 701 – 722, doi:10.1175/BAMS-D-13-00164.1.
- Houze, R. A., 2010: Clouds in tropical cyclones. *Monthly Weather Review*, **138**, 293–344, doi:10.1175/2009MWR2989.1.
- Houze, R. A. and D. D. Churchill, 1984: Microphysical structure of winter monsoon cloud clusters. *Journal of Atmospheric Sciences*, **41**, 3405 – 3411, doi:10.1175/1520-0469(1984)041<3405:MSOWMC>2.0.CO;2.
- Houze, R. A., F. D. Marks, and R. A. Black, 1992: Dual-Aircraft Investigation of the Inner Core of Hurricane Norbert. Part II: Mesoscale Distribution of Ice Particles.
- Huang, H., Q. Li, K. Zhao, H. Dai, J. Ming, X. Fan, Y. Xu, Y. Duan, W.-C. Lee, and F. Zheng, 2022: Microphysical characteristics of the phase-locking vrw-induced asymmetric convection in the outer eyewall of super typhoon lekima (2019). *Geophysical Research Letters*, **49**, e2021GL096869, doi:<https://doi.org/10.1029/2021GL096869>.
- Iacono, M. J., J. S. Delamere, E. J. Mlawer, M. W. Shephard, S. A. Clough, and W. D. Collins, 2008: Radiative forcing by long-lived greenhouse gases: Calculations with the aer radiative transfer models. *Journal of Geophysical Research: Atmospheres*, **113**, doi:<https://doi.org/10.1029/2008JD009944>.
- Jensen, A. A. and J. Y. Harrington, 2015: Modeling ice crystal aspect ratio evolution during riming: A single-particle growth model. *J. Atmos. Sci.*, **72**, 2569–2590, doi:10.1175/JAS-D-14-0297.1.
- Jensen, A. A., J. Y. Harrington, H. Morrison, and J. A. Milbrandt, 2017: Predicting ice shape evolution in a bulk microphysics model. *J. Atmos. Sci.*, **74**, 2081–2104, doi:10.1175/JAS-D-16-0350.1.
- Jensen, E. J., S. C. van den Heever, and L. D. Grant, 2018: The Life Cycles of Ice Crystals Detrained From the Tops of Deep Convection. *J. Geophys. Res. Atmos.*, **123**, 9624–9634, doi:10.1029/2018JD028832.
- Jones, S. C., 1995: The evolution of vortices in vertical shear. I: Initially barotropic vortices. *Quarterly Journal of the Royal Meteorological Society*, **121**, 821–851, doi:10.1002/qj.49712152406.

- Khain, A. P., K. D. Beheng, A. Heymsfield, A. Korolev, S. O. Krichak, Z. Levin, M. Pinsky, V. Phillips, T. Prabhakaran, A. Teller, S. C. van den Heever, and J.-I. Yano, 2015: Representation of microphysical processes in cloud-resolving models: Spectral (bin) microphysics versus bulk parameterization. *Reviews of Geophysics*, **53**, 247–322, doi:10.1002/2014RG000468.
- Kumjian, M. R. and K. Lombardo, 2020: A hail growth trajectory model for exploring the environmental controls on hail size: Model physics and idealized tests. *Journal of the Atmospheric Sciences*, **77**, 2765 – 2791, doi:10.1175/JAS-D-20-0016.1.
- Laurencin, C. N., A. C. Didlake Jr., J. Y. Harrington, and A. A. Jensen, 2022: Evaluating an ice crystal trajectory growth (ictg) model on a quasi-idealized simulation of a squall line. *Journal of Advances in Modeling Earth Systems*, **14**, e2021MS002764, doi:<https://doi.org/10.1029/2021MS002764>, e2021MS002764 2021MS002764.
- Laurencin, C. N., A. C. Didlake Jr., S. D. Loeffler, M. R. Kumjian, and G. M. Heymsfield, 2020: Hydrometeor size sorting in the asymmetric eyewall of hurricane matthew (2016). *Journal of Geophysical Research: Atmospheres*, **125**, e2020JD032671, doi:<https://doi.org/10.1029/2020JD032671>, e2020JD032671 2020JD032671.
- Libbrecht, K. G., 2005: The physics of snow crystals. *Report on Progress in Physics*, **68**, doi:10.1088/0034-4885/68/4/R03.
- Marks, F. D. and R. A. Houze, 1987: Inner core structure of hurricane alicia from airborne doppler radar observations. *J. Atmos. Sci.*, **44**, 1296–1317.
- Mason, B. J., 1994: The shapes of snow crystals—fitness for purpose? *Quarterly Journal of the Royal Meteorological Society*, **120**, 849–860, doi:<https://doi.org/10.1002/qj.49712051805>.
- May, P. T., J. D. Kepert, and T. D. Keenan, 2008: Polarimetric radar observations of the persistently asymmetric structure of tropical cyclone ingrid. *Monthly Weather Review*, **136**, 616 – 630, doi:10.1175/2007MWR2077.1.
- Morrison, H. and J. A. Milbrandt, 2015: Parameterization of cloud microphysics based on the prediction of bulk ice particle properties. Part I: Scheme description and idealized tests. *J. Atmos. Sci.*, **72**, 287–311, doi:10.1175/JAS-D-14-0065.1.
- Morrison, H., J. A. Milbrandt, G. H. Bryan, K. Ikeda, S. A. Tessendorf, and G. Thompson, 2015: Parameterization of cloud microphysics based on the prediction of bulk ice particle properties. Part II: Case study comparisons with observations and other schemes. *J. Atmos. Sci.*, **72**, 312–339, doi:10.1175/JAS-D-14-0066.1.
- Morrison, H., S. A. Tessendorf, K. Ikeda, and G. Thompson, 2012: Sensitivity of a simulated midlatitude squall line to parameterization of raindrop breakup. *Mon. Wea. Rev.*, **140**, 2437–2460, doi:10.1175/MWR-D-11-00283.1.

- Morrison, H., G. Thompson, and V. Tatarki, 2009: Impact of cloud microphysics on the development of trailing stratiform precipitation in a simulated squall line: Comparison of one- and two-moment schemes. *Mon. Wea. Rev.*, **137**, 991–1007, doi:10.1175/2008MWR2556.1.
- Morrison, H., M. van Lier-Walqui, A. M. Fridlind, W. W. Grabowski, J. Y. Harrington, C. Hoose, A. Korolev, M. R. Kumjian, J. A. Milbrandt, H. Pawlowska, D. J. Posselt, O. P. Prat, K. J. Reimel, S. I. Shima, B. van Diedenhoven, and L. Xue, 2020: Confronting the Challenge of Modeling Cloud and Precipitation Microphysics. *J. Adv. Model. Earth Syst.*, **12**, 68, doi:10.1029/2019MS001689.
- Pasquier, J. T., J. Henneberger, A. Korolev, F. Ramelli, J. Wieder, A. Lauber, G. Li, R. O. David, T. Carlsen, R. Gierens, M. Maturilli, and U. Lohmann, 2023: Understanding the history of two complex ice crystal habits deduced from a holographic imager. *Geophysical Research Letters*, **50**, e2022GL100247, doi:<https://doi.org/10.1029/2022GL100247>, e2022GL100247 2022GL100247.
- Rojas, B., A. Didlake, J. Harrington, and C. Laurencin, 2025: Using a novel ice crystal trajectory growth (ictg) model to understand ice in a tropical cyclone eyewall. *Journal of Geophysical Research: Atmospheres*, Submitted.
- Rojas, B. S., A. C. Didlake, and J. A. Zhang, 2024: Asymmetries during eyewall replacement cycles of hurricane ivan (2004). *Monthly Weather Review*, **152**, 1741 – 1761, doi:10.1175/MWR-D-23-0129.1.
- Sheridan, L. M., J. Y. Harrington, D. Lamb, and K. Sulia, 2009: Influence of ice crystal aspect ratio on the evolution of ice size spectra during vapor depositional growth. *Journal of the Atmospheric Sciences*, **66**, 3732 – 3743, doi:10.1175/2009JAS3113.1.
- Skamarock, W. C., J. B. Klemp, J. Dudhia, D. O. Gill, D. M. Barker, M. G. Duda, X.-Y. Huang, W. Wang, J. G. Powers, et al., 2008: A description of the advanced research wrf version 3. *NCAR technical note*, **475**, 10–5065.
- Skofronick-Jackson, G., M. Kulie, L. Milani, S. J. Munchak, N. B. Wood, and V. Levizzani, 2019: Satellite estimation of falling snow: A global precipitation measurement (gpm) core observatory perspective. *Journal of Applied Meteorology and Climatology*, **58**, 1429 – 1448, doi:10.1175/JAMC-D-18-0124.1.
- Thompson, G., P. R. Field, R. M. Rasmussen, and W. D. Hall, 2008: Explicit forecasts of winter precipitation using an improved bulk microphysics scheme. part ii: Implementation of a new snow parameterization. *Monthly Weather Review*, **136**, 5095 – 5115, doi:10.1175/2008MWR2387.1.
- Willoughby, H. E., 1998: Tropical cyclone eye thermodynamics. *Monthly Weather Review*, **126**, 3053 – 3067, doi:10.1175/1520-0493(1998)126<3053:TCET>2.0.CO;2.

Woods, C. P., M. T. Stoelinga, and J. D. Locatelli, 2007: The improve-1 storm of 1–2 february 2001. part iii: Sensitivity of a mesoscale model simulation to the representation of snow particle types and testing of a bulk microphysical scheme with snow habit prediction. *Journal of the Atmospheric Sciences*, **64**, 3927 – 3948, doi:10.1175/2007JAS2239.1.

Zhang, C. and J. Y. Harrington, 2014: Including surface kinetic effects in simple models of ice vapor diffusion. *J. Atmos. Sci.*, **71**, 372–390, doi:10.1175/JAS-D-13-0103.1.

Zhang, Y.-F., C. M. Bitz, J. L. Anderson, N. S. Collins, T. J. Hoar, K. D. Raeder, and E. Blanchard-Wrigglesworth, 2021: Estimating parameters in a sea ice model using an ensemble kalman filter. *The Cryosphere*, **15**, 1277–1284, doi:10.5194/tc-15-1277-2021.